

# *Euclid*: Optimising tomographic redshift binning for 3×2pt power spectrum constraints on dark energy<sup>★</sup>

J. H. W. Wong<sup>★\*1</sup>, M. L. Brown<sup>1</sup>, C. A. J. Duncan<sup>1</sup>, A. Amara<sup>2</sup>, S. Andreon<sup>3</sup>, C. Baccigalupi<sup>4,5,6,7</sup>, M. Baldi<sup>8,9,10</sup>, S. Bardelli<sup>9</sup>, D. Bonino<sup>11</sup>, E. Branchini<sup>12,13,3</sup>, M. Brescia<sup>14,15,16</sup>, J. Brinchmann<sup>17,18</sup>, A. Caillat<sup>19</sup>, S. Camera<sup>20,21,11</sup>, V. Capobianco<sup>11</sup>, C. Carbone<sup>22</sup>, J. Carretero<sup>23,24</sup>, S. Casas<sup>25,26</sup>, M. Castellano<sup>27</sup>, G. Castignani<sup>9</sup>, S. Cavuoti<sup>15,16</sup>, A. Cimatti<sup>28</sup>, C. Colodro-Conde<sup>29</sup>, G. Congedo<sup>30</sup>, C. J. Conselice<sup>1</sup>, L. Conversi<sup>31,32</sup>, Y. Copin<sup>33</sup>, F. Courbin<sup>34,35</sup>, H. M. Courtois<sup>36</sup>, A. Da Silva<sup>37,38</sup>, H. Degaudenzi<sup>39</sup>, G. De Lucia<sup>5</sup>, A. M. Di Giorgio<sup>40</sup>, J. Dinis<sup>37,38</sup>, F. Dubath<sup>39</sup>, X. Dupac<sup>32</sup>, S. Dusini<sup>41</sup>, M. Farina<sup>40</sup>, S. Farrens<sup>42</sup>, F. Faustini<sup>43,27</sup>, S. Ferriol<sup>33</sup>, M. Frailis<sup>5</sup>, E. Franceschi<sup>9</sup>, S. Galeotta<sup>5</sup>, K. George<sup>44</sup>, W. Gillard<sup>45</sup>, B. Gillis<sup>30</sup>, C. Giocoli<sup>9,10</sup>, A. Grazian<sup>46</sup>, F. Grupp<sup>47,44</sup>, L. Guzzo<sup>48,3</sup>, S. V. H. Haugan<sup>49</sup>, W. Holmes<sup>50</sup>, I. Hook<sup>51</sup>, F. Hormuth<sup>52</sup>, A. Hornstrup<sup>53,54</sup>, S. Ilic<sup>55,56</sup>, K. Jahnke<sup>57</sup>, M. Jhabvala<sup>58</sup>, E. Keihänen<sup>59</sup>, S. Kermiche<sup>45</sup>, A. Kiessling<sup>50</sup>, B. Kubik<sup>33</sup>, M. Kunz<sup>60</sup>, H. Kurki-Suonio<sup>61,62</sup>, S. Ligi<sup>11</sup>, P. B. Lilje<sup>49</sup>, V. Lindholm<sup>61,62</sup>, I. Lloro<sup>63</sup>, G. Mainetti<sup>64</sup>, E. Maiorano<sup>9</sup>, O. Mansutti<sup>5</sup>, O. Marggraf<sup>65</sup>, K. Markovic<sup>50</sup>, M. Martinelli<sup>27,66</sup>, N. Martinet<sup>19</sup>, F. Marulli<sup>67,9,10</sup>, R. Massey<sup>68</sup>, E. Medinaceli<sup>9</sup>, S. Mei<sup>69</sup>, M. Melchior<sup>70</sup>, Y. Mellier<sup>71,72</sup>, M. Meneghetti<sup>9,10</sup>, E. Merlin<sup>27</sup>, G. Meylan<sup>73</sup>, M. Moresco<sup>67,9</sup>, L. Moscardini<sup>67,9,10</sup>, C. Neissner<sup>74,24</sup>, S.-M. Niemi<sup>75</sup>, C. Padilla<sup>74</sup>, S. Paltani<sup>39</sup>, F. Pasian<sup>5</sup>, K. Pedersen<sup>76</sup>, V. Pettorino<sup>75</sup>, S. Pires<sup>42</sup>, G. Polenta<sup>43</sup>, M. Poncet<sup>77</sup>, L. A. Popa<sup>78</sup>, F. Raison<sup>47</sup>, A. Renzi<sup>79,41</sup>, J. Rhodes<sup>50</sup>, G. Riccio<sup>15</sup>, E. Romelli<sup>5</sup>, M. Roncarelli<sup>9</sup>, E. Rossetti<sup>8</sup>, R. Saglia<sup>44,47</sup>, Z. Sakr<sup>80,56,81</sup>, A. G. Sánchez<sup>47</sup>, D. Sapone<sup>82</sup>, B. Sartoris<sup>44,5</sup>, P. Schneider<sup>65</sup>, T. Schrabback<sup>83</sup>, A. Secroun<sup>45</sup>, G. Seidel<sup>57</sup>, S. Serrano<sup>84,85,86</sup>, C. Sirignano<sup>79,41</sup>, G. Sirri<sup>10</sup>, L. Stanco<sup>41</sup>, J. Steinwagner<sup>47</sup>, P. Tallada-Crespi<sup>23,24</sup>, A. N. Taylor<sup>30</sup>, I. Tereno<sup>37,87</sup>, R. Toledo-Moreo<sup>88</sup>, F. Torradeflot<sup>24,23</sup>, I. Tutusaus<sup>56</sup>, L. Valenziano<sup>9,89</sup>, T. Vassallo<sup>44,5</sup>, G. Verdoes Kleijn<sup>90</sup>, A. Veropalumbo<sup>3,13,91</sup>, Y. Wang<sup>92</sup>, J. Weller<sup>44,47</sup>, G. Zamorani<sup>9</sup>, E. Zucca<sup>9</sup>, C. Burigana<sup>93,89</sup>, M. Calabrese<sup>94,22</sup>, A. Pezzotta<sup>47</sup>, V. Scottez<sup>71,95</sup>, A. Spurio Mancini<sup>96</sup>, and M. Viel<sup>4,5,7,6,97</sup>

(Affiliations can be found after the references)

January 14, 2025

## ABSTRACT

The tomographic approach to analyse the 3×2pt signal involves dividing the observed galaxy sample into a configuration of redshift bins. We present a simulation-based method to explore the optimum tomographic binning strategy for *Euclid*, focusing on the expected configuration of its first major data release (DR1). To do this, we 1) simulate a *Euclid*-like observation and generate mock shear catalogues from multiple realisations of the 3×2pt fields on the sky, and 2) measure the 3×2pt Pseudo- $C_\ell$  power spectra for a given tomographic configuration and derive the constraints that they place on the standard dark energy equation of state parameters ( $w_0, w_a$ ). For a simulation including Gaussian-distributed photometric redshift uncertainty and shape noise under a  $\Lambda$ CDM cosmology, we find that bins equipopulated with galaxies yield the best constraints on ( $w_0, w_a$ ) for an analysis of the full 3×2pt signal, or the angular clustering component only. For the cosmic shear component, the optimum ( $w_0, w_a$ ) constraints are achieved by bins equally spaced in fiducial comoving distance. However, the advantage with respect to alternative binning choices is only a few percent in the size of the  $1\sigma$  ( $w_0, w_a$ ) contour, and we conclude that the cosmic shear is relatively insensitive to the binning methodology. We find that the information gain extracted on ( $w_0, w_a$ ) for any 3×2pt component starts to saturate at  $\geq 7$ –8 bins. Any marginal gains resulting from a greater number of bins is likely to be limited by additional uncertainties present in a real measurement, and the increasing demand for accuracy of the covariance matrix. Finally, we consider a 5% contamination from catastrophic photometric redshift outliers and find that, if these errors are not mitigated in the analysis, the bias induced in the 3×2pt signal for 10 equipopulated bins results in dark energy constraints that are inconsistent with the fiducial  $\Lambda$ CDM cosmology at  $> 5\sigma$ .

**Key words.** Cosmology: observations – dark energy – cosmological parameters – Methods: statistical – Gravitational lensing: weak

## 1. Introduction

The weak gravitational lensing of galaxies by the large-scale structure in the Universe, known as cosmic shear, has emerged as a key tool for cosmology due to its ability to probe the evolution of matter through cosmic time. This property has allowed weak

lensing analyses (see e.g. Kilbinger 2015 for a review) to be used to constrain the nature of dark energy, proposed as the origin of the observed accelerated expansion of the Universe (Riess et al. 1998, Schmidt et al. 1998, Perlmutter et al. 1999).

Surveys such as *Euclid* (Laureijs et al. 2011, *Euclid Collaboration: Mellier et al. 2024*), the forthcoming *Nancy Grace Roman Space Telescope* (Spergel et al. 2015) and the Vera C. Rubin Observatory Legacy Survey of Space and Time (*LSST Science*

<sup>★</sup> This paper is published on behalf of the Euclid Consortium.

<sup>\*\*</sup> e-mail: jonathan.wong-6@postgrad.manchester.ac.uk

Collaboration et al. 2009), will provide samples of over 1 billion galaxies, and are expected to offer at least an order of magnitude improvement in the precision of cosmic shear measurements over current experiments. These data will be used to investigate the extent to which dark energy can be described as a time-evolving fluid contributing to the mass-energy budget of the Universe. *Euclid* in particular will target constraints on a  $w_0w_a$ CDM cosmology, whereby the dark energy equation of state parameter  $w$  is assumed to take the functional form  $w = w_0 + (1 - a)w_a$  (Laureijs et al. 2011), where  $a$  is the scale factor.

Intrinsic to the weak lensing method is the analysis of the 3-dimensional radial distribution of matter in the Universe, traced by the galaxies observed in the survey. While a cosmic shear study can employ the ‘3D weak lensing’ analysis technique (Heavens 2003, Kitching et al. 2014, Spurio Mancini et al. 2018) whereby the shear field is expanded radially in spherical Bessel functions, the common method, known as tomography, involves subdividing the observed galaxy population into binned samples at different distances. This technique effectively compresses the 3-dimensional cosmological information into a number of slices, through which a 2-dimensional 2-point analysis of the projected galaxy images is used to recover the radial shear field (Hu 1999).

Comparatively, 3D weak lensing measurements (Castro et al. 2005, Kitching et al. 2007) naturally offer more statistical power for cosmological parameter constraints. However the information gain is dependent on the chosen parameter(s) and it has been demonstrated (e.g. Hu 2002; Jain & Taylor 2003; Huterer 2002; Schrabback et al. 2010; Benjamin et al. 2013; Taylor et al. 2018b) that the tomographic weak lensing approach recovers the majority of the cosmological information required to make measurements of dark energy with the benefit of a significant reduction in computational cost. Indeed, the current generation of surveys such as the Dark Energy Survey (DES; Abbott et al. 2022), the Kilo Degree Survey (KiDS; Hildebrandt et al. 2017), and the Subaru Hyper Suprime-Cam (HSC; Hikage et al. 2019) have consistently utilised weak lensing tomography to obtain constraints on parameters such as the matter density,  $\Omega_m$ , the amplitude of matter fluctuations on scales of  $8 h^{-1}$  Mpc,  $\sigma_8$ , and the dark energy equation of state parameter,  $w$ . These analyses provide complementary measurements to constraints derived from alternative probes such as Type Ia supernovae (e.g. Brout et al. 2022), the cosmic microwave background (CMB, e.g. Planck Collaboration: Aghanim et al. 2020) and baryon acoustic oscillations (BAO, e.g. Alam et al. 2017).

Notably, the DES collaboration (Abbott et al. 2023) have constrained the dark energy ( $w_0, w_a$ ) parameters using a tomographic analysis of the  $3 \times 2$ pt signal (the joint data vector of cosmic shear, angular galaxy clustering and their cross-correlation, see Sect. 3.1). When combining the  $3 \times 2$ pt signal with *Planck* temperature and *E*-mode polarisation observables (Planck Collaboration: Aghanim et al. 2020), BAO results from eBOSS (Ahumada et al. 2020) and the Pantheon SNe Ia sample (Scolnic et al. 2018), they found  $(w_0, w_a) = (-0.95 \pm 0.08, -0.4^{+0.4}_{-0.3})$  which is consistent with a  $\Lambda$ CDM model at  $1\sigma$ .

Comparatively, the Pantheon+ analysis of a larger sample of distinct SNe Ia (see Brout et al. 2022 and references therein) have found  $(w_0, w_a) = (-0.841^{+0.066}_{-0.061}, -0.65^{+0.28}_{-0.32})$  when combining with *Planck* and BAO, which is moderately consistent with the cosmological constant at  $2\sigma$ . In addition, the Dark Energy Spectroscopic Instrument (DESI Collaboration et al. 2016, DESI Collaboration et al. 2024) has found support for  $w_0 > -1, w_a < 0$  when combining BAO and *Planck* CMB data, which is inconsistent with  $\Lambda$ CDM at  $\geq 2.5\sigma$ .

It will be the target of *Euclid* to provide a  $\sim 2\%$  and  $\sim 10\%$  measurement on  $w_0$  and  $w_a$  respectively (Laureijs et al. 2011), which will help to further investigate the nature of dark energy and the validity of the standard  $\Lambda$ CDM model.

The structure of this paper is as follows. In Sect. 2 we discuss previous attempts to investigate tomographic binning strategies for weak lensing surveys, and highlight the need to determine an appropriate strategy for *Euclid*. In Sects. 3, 4 we review the analytical estimators used to measure the  $3 \times 2$ pt signal, and present our method to simulate mock Stage IV-like galaxy catalogues. In Sects. 5, 6 we discuss the inference method that we use to derive constraints on the  $(w_0, w_a)$  parameters from the  $3 \times 2$ pt signal, and explore these constraints for different tomographic binning strategies applied to our mock catalogues. In Sect. 7 we explore the effects of catastrophic photometric redshift uncertainties, and in Sect. 8 we discuss the overall conclusions of our study to determine an optimum tomographic binning method. Finally, in the Appendix we review the validation testing we have conducted for our simulation method, and discuss finer details on the modelling and computational choices that we have implemented in this work.

## 2. Motivations

To construct a tomographic measurement, two analysis choices must be made: the number of bins to split the observed galaxy sample into; and how to determine the bin boundaries along the radial (line-of-sight) direction. Each of these choices are governed by both scientific and practical considerations.

In regard to choosing the number of tomographic bins, it is generally expected that a greater number of bins will increase the information captured in a shear analysis, but require a larger computational cost. However, there will be a point at which the information gain starts to saturate, since more sample bins increases the Poisson shot noise per bin, which will dominate over the underlying cosmological shear signal of interest (see also Sect. 3 for more details). Additionally, the cosmological volume enclosed by a single bin reduces as a larger number of bins is used, resulting in a comparatively lower gain in information, as the lensing signal over a given bin changes less.

Several studies conducted to determine the ‘optimum’ tomography for a Stage IV-like weak lensing survey have explored this issue. For example, Taylor et al. (2018a) use a principal component analysis to compare the suitability of a range of tomographic binning strategies with respect to the 3D cosmic shear method. For a *Euclid*-like weak lensing signal, they find that  $\sim 10$  tomographic bins with equal populations of galaxies can sufficiently capture the majority ( $\sim 97\%$ ) of the cosmological information of the 3D approach, but the tomographic method starts to fail at higher redshifts due to information loss and computational cost. Comparatively, a tomographic setup with bins equally spaced in redshift does not capture as much information as the equipopulated case for a small number of bins, but can extract  $\sim 99\%$  of the information with respect to the 3D method for a large number of bins ( $\sim 50$ ). Regardless of binning choice, the computational advantage of tomography is highlighted with respect to a 3D analysis.

This result is consistent with Sipp et al. (2021), who explore different tomographic strategies to assess the statistical properties of a predicted *Euclid*-like cosmic shear signal. For a range of science metrics, including minimising the uncertainties on individual cosmological parameter constraints; and the optimisation of the *Euclid* dark energy figure of merit (Euclid Collaboration: Blanchard et al. 2020), they find that the optimum tomographic

configuration is very close to the equipopulated scenario, with a small number of bins (4–5) sufficient for the cosmological analysis.

Contrastingly, [Kitching et al. \(2019\)](#) use a self organising map technique (SOM; [Kohonen 1990](#)) to define bin boundaries in photometric colour space, while optimising the signal-to-noise ratio (SNR) on the dark energy equation of state parameter  $w_0$  measured from the cosmic shear power spectrum. For a small number of bins ( $< 5$ ), the best performing binning methodology identified by the SOM is found to be a close approximation of the case where the bins are defined to have equal width in redshift.

This issue is further complicated if a ‘3×2pt’ analysis of the data is targeted (see Sect. 3.1), whereby the shear signal is combined with the tomographic galaxy number density (angular clustering) and galaxy-galaxy lensing (cross-correlation of weak lensing and angular clustering) signals into a joint data vector. The full 3×2pt data vector will offer more constraining power than a shear-only analysis (see e.g. [Tutusaus et al. 2020](#)). However, the choice of an appropriate tomographic binning configuration may also depend on which cosmological parameter is being targeted and which part of the data vector is most sensitive to the corresponding science case.

In particular, by considering the photometric redshift estimation techniques for *Euclid*, [Euclid Collaboration: Pocino et al. \(2021\)](#) find that for a galaxy clustering and galaxy-galaxy lensing analysis, tomographic bins equally spaced in redshift yield a higher dark energy figure of merit (FOM) than equipopulated bins, and a relatively large number of bins (13) maximises the amount of cosmological information extracted.

Additionally, [Zuntz et al. \(2021\)](#) have coordinated a tomography challenge in which a range of tomographic binning configurations, guided by machine learning approaches on a test sample, were proposed by the community to target a variety of metrics such as the 3×2pt power spectra SNR and dark energy FOM. The findings suggest that the optimum tomographic binning setup used for the analysis is strongly dependent on both the chosen 3×2pt observable, and the specific cosmological parameter FOM that is targeted. Overall however, a source galaxy distribution which is split into redshift bins that are equally spaced in fiducial comoving distance was found to be a good general choice.

It is clear that these studies reach a variety of different conclusions, and in addition they are not all performed for the same target survey setup. This makes their use for choosing an optimum binning scheme for *Euclid* difficult. Hence, the aim of this work is to present an alternative method to explore a range of 3×2pt tomographic configurations, and investigate an optimum tomographic binning approach for the specific survey characteristics expected for the analysis of *Euclid*’s first data release (DR1).

We construct a cosmological simulation pipeline that generates full *Euclid*-like cosmic shear catalogues realised on the sky from a given fiducial cosmology, with realistic observational uncertainties such as photo- $z$  errors and shape noise injected into the catalogue observables. From our simulated catalogues we measure the 3×2pt signal and compare constraints on the dark energy equation of state for each tomographic setup chosen, which will help to further identify the optimum configuration for the analysis of 3×2pt cosmological signals in the *Euclid* survey.

Our simulation pipeline includes the following stages.

1. The sampling of an observed galaxy population from a predicted *Euclid*-like galaxy redshift distribution and spatial number density.

2. The calculation of a theoretical 3×2pt signal over a given redshift range and fiducial cosmology.
3. Simulations of the correlated cosmic shear and galaxy density fields on the sky as a set of 2D maps that approximates the 3D evolution of the 3×2pt signal over time.
4. The sampling of galaxy angular positions and weak lensing observables from the density and shear fields respectively.
5. The injection of observational uncertainties from photo- $z$  estimation and galaxy shape noise into the individual galaxies to generate a mock catalogue mimicking a realistic survey.

We provide a full description of this simulation method and each stage in Sect. 4. We note that the previously discussed tomography studies typically focus on using numerical methods to explore a theoretical shear signal. In comparison, we highlight that our method offers the advantage of imitating a realistic survey observation and measuring the corresponding 3×2pt signal from an underlying cosmology, which relies on fewer assumptions and provides a more direct and realistic framework with which to investigate the cosmological impact of different tomographic strategies.

### 3. Background and theory

#### 3.1. Cosmic shear and the 3×2pt signal

Gravitational lensing occurs when the foreground potential of a massive object distorts the light observed from a background source. In the regime of weak lensing where the distortion effects are small, at percent level, the phenomenon leads to subtle changes to a background galaxy’s size and shape which can be described using the convergence  $\kappa$  (spin-0 quantity) and shear  $\gamma$  (spin-2 quantity) respectively.

For a population of multiple background galaxies, weak lensing leads to correlations in the distortions of individual galaxy shapes. Using tomography, the galaxy sample is split into a set of redshift bins and the cosmic shear signal is then measured using the angular power spectrum under the Limber approximation ([Limber 1953](#), [LoVerde & Afshordi 2008](#)) as  $C_{ij}(\ell)$  where  $i, j$  denote the pairs of redshift bins in the sample. Explicitly, for a flat Universe the tomographic shear power spectrum,  $C_{ij}^{\gamma\gamma}(\ell)$ , is given by (see e.g. [Bartelmann & Schneider 2001](#) for a derivation of the following expressions)

$$C_{ij}^{\gamma\gamma}(\ell) = \frac{9}{4} \Omega_m^2 \left(\frac{H_0}{c}\right)^4 \int_0^{\chi_H} d\chi \frac{q_i^k(\chi) q_j^k(\chi)}{\chi^2} P_\delta\left(\frac{\ell + 1/2}{\chi}, \chi\right), \quad (1)$$

where we take the matter density parameter at the present day,  $\Omega_m = 0.3$  and the Hubble constant,  $H_0 = 70 \text{ km s}^{-1} \text{ Mpc}^{-1}$  throughout this work. Additionally, the comoving radial coordinate  $\chi$  is integrated up to  $\chi_H$ , the comoving distance to the cosmic horizon,  $a$  is the scale factor,  $P_\delta$  is the matter power spectrum, and  $q_i^k(\chi)$  is the lensing efficiency,

$$q_i^k(\chi) = \frac{\chi}{a(\chi)} \int_\chi^{\chi_H} d\chi' \frac{n_i(z) dz/d\chi'}{\bar{n}_i} \frac{\chi' - \chi}{\chi'}, \quad (2)$$

which describes the redshift distribution of the background galaxies  $n_i(z)$  weighted by the angular number density,

$$\bar{n}_i = \int_0^\infty dz n_i(z), \quad (3)$$

where the redshift  $z = z(\chi)$  and  $i$  denotes a given tomographic bin. One can also consider a full 3×2pt analysis, using the galaxy

angular positions on the sky,  $\delta_g(\boldsymbol{\theta})$ , and the corresponding galaxy clustering radial kernel  $q_i^{\delta_g}$ ,

$$q_i^{\delta_g}(k, \chi) = b_i(k, z) n_i(z) \frac{dz}{d\chi}, \quad (4)$$

where  $b_i(k, z)$  is the galaxy bias in tomographic bin  $i$ , which describes the spatial relation between the underlying matter field and the observed distribution of galaxies as a function of redshift and scale  $k$ , where  $k = (\ell + 1/2)/\chi$ .

In addition to weak lensing, the  $3 \times 2$ pt signal consists of the galaxy clustering angular power spectrum,

$$C_{ij}^{\delta_g \delta_g}(\ell) = \int_0^{\chi_H} d\chi \frac{q_i^{\delta_g}(\frac{\ell+1/2}{\chi}, \chi) q_j^{\delta_g}(\frac{\ell+1/2}{\chi}, \chi)}{\chi^2} P_\delta\left(\frac{\ell+1/2}{\chi}, \chi\right), \quad (5)$$

and the cross correlation of the clustering and shear kernels, the galaxy-galaxy lensing power spectrum  $C_{ij}^{\delta_g \gamma}(\ell)$ ,

$$C_{ij}^{\delta_g \gamma}(\ell) = \frac{3}{2} \Omega_m \left(\frac{H_0}{c}\right)^2 \times \int_0^{\chi_H} d\chi \frac{q_i^{\delta_g}(\frac{\ell+1/2}{\chi}, \chi) q_j^\gamma(\chi)}{\chi^2} P_\delta\left(\frac{\ell+1/2}{\chi}, \chi\right). \quad (6)$$

We note that these expressions for the  $3 \times 2$ pt signal do not include the effects of intrinsic alignments, which we do not consider in this work.

### 3.2. Estimators for the $3 \times 2$ pt signal

#### 3.2.1. Cosmic shear estimators

The shear,  $\gamma(\boldsymbol{\theta})$ , which describes how weak lensing ‘stretches’ and ‘rotates’ an image is a spin-2 field, and can therefore be written as a complex quantity,

$$\gamma(\boldsymbol{\theta}) = \gamma_1(\boldsymbol{\theta}) + i\gamma_2(\boldsymbol{\theta}). \quad (7)$$

On the full sky, the shear signal can be expressed in spherical harmonic space via the  ${}_{\pm 2}Y_{\ell,m}(\boldsymbol{\theta})$  spin-2 harmonics defined on the sphere,

$$\gamma(\boldsymbol{\theta}) = \sum_{\ell,m} {}_{\pm 2}\tilde{\gamma}_{\ell,m} {}_{\pm 2}Y_{\ell,m}(\boldsymbol{\theta}), \quad (8)$$

where the  $\tilde{\gamma}_{\ell,m}$  coefficients can be expressed using the gradient  $E$ - and curl  $B$ -modes analogous to the  $Q$  and  $U$  Stokes parameters for an electromagnetic field (Crittenden et al. 2002, Kamionkowski et al. 1998, Stebbins 1996, Kaiser 1992),

$${}_{\pm 2}\tilde{\gamma}_{\ell,m} = E_{\ell,m} \pm iB_{\ell,m} = \int (\gamma_1 \pm i\gamma_2) {}_{\pm 2}Y_{\ell,m}^*(\boldsymbol{\theta}) d\boldsymbol{\theta}, \quad (9)$$

and the coefficients for each mode are given by

$$E_{\ell,m} = \frac{1}{2} \int [\gamma(\boldsymbol{\theta}) {}_{+2}Y_{\ell,m}^*(\boldsymbol{\theta}) + \gamma^*(\boldsymbol{\theta}) {}_{-2}Y_{\ell,m}^*(\boldsymbol{\theta})] d\boldsymbol{\theta}, \quad (10)$$

$$B_{\ell,m} = -\frac{i}{2} \int [\gamma(\boldsymbol{\theta}) {}_{+2}Y_{\ell,m}^*(\boldsymbol{\theta}) - \gamma^*(\boldsymbol{\theta}) {}_{-2}Y_{\ell,m}^*(\boldsymbol{\theta})] d\boldsymbol{\theta}, \quad (11)$$

where each of these integrals are done over the full sphere. From the harmonic coefficients, we define the  $E$ -mode,  $B$ -mode, and  $EB$  angular power spectra as

$$\langle E_{\ell,m} E_{\ell',m'}^* \rangle = \delta_{\ell\ell'} \delta_{mm'} C^{EE}(\ell), \quad (12)$$

$$\langle B_{\ell,m} B_{\ell',m'}^* \rangle = \delta_{\ell\ell'} \delta_{mm'} C^{BB}(\ell), \quad (13)$$

$$\langle E_{\ell,m} B_{\ell',m'}^* \rangle = \delta_{\ell\ell'} \delta_{mm'} C^{EB}(\ell), \quad (14)$$

where  $\delta_{XY}$  is the Kronecker delta and the triangular brackets denote an ensemble average over many realisations. Since we only observe one Universe and are limited by the number of  $m$  modes available, each  $C(\ell)$  value is distributed among  $2\ell + 1$  degrees of freedom. Consequently, we can only measure an estimate of the true power spectrum,  $\hat{C}(\ell)$ , which for the given tomographic bins  $i, j$  we define for the shear modes as

$$\hat{C}_{ij}^{EE}(\ell) = \frac{1}{2\ell + 1} \sum_{m=-\ell}^{+\ell} E_{\ell,m}^{(i)} E_{\ell,m}^{(j)*}, \quad (15)$$

$$\hat{C}_{ij}^{BB}(\ell) = \frac{1}{2\ell + 1} \sum_{m=-\ell}^{+\ell} B_{\ell,m}^{(i)} B_{\ell,m}^{(j)*}, \quad (16)$$

$$\hat{C}_{ij}^{EB}(\ell) = \frac{1}{2\ell + 1} \sum_{m=-\ell}^{+\ell} E_{\ell,m}^{(i)} B_{\ell,m}^{(j)*}. \quad (17)$$

In the weak lensing regime assuming the Born approximation, it has been shown that to leading order the shear field contains no power arising from the  $B$ -mode curl component (Hilbert et al. 2009, Krause & Hirata 2010), and the coefficient  $B_{\ell,m}$  is taken as zero (e.g. Giocoli et al. 2016).

Hence the shear signal is typically fully characterised by the  $E$ -mode, which we use to estimate the theoretical shear power spectrum in this work, i.e.  $C_{ij}^{\gamma\gamma}(\ell) = \langle \hat{C}_{ij}^{EE}(\ell) \rangle$ . The  $B$ -mode power spectrum can be used as an important null test for systematics.

#### 3.2.2. Galaxy clustering estimators

The angular galaxy clustering signal is estimated using the normalised galaxy number count on a pixelised sky, which traces the underlying matter distribution. For the tomographic bin  $i$  we form the real-space overdensity estimator:

$$\hat{\delta}_g^{(i)}(\boldsymbol{\theta}) = \frac{n_i^p(\boldsymbol{\theta}) - \bar{n}_i^p}{\bar{n}_i^p}, \quad (18)$$

where  $n_i^p(\boldsymbol{\theta})$  is the per-pixel integer galaxy count in the redshift bin and  $\bar{n}_i^p$  is the average number of galaxies observed per pixel in the same bin.

Analogous to the shear field, the measured galaxy overdensity field can be represented in spherical harmonic space via the overdensity coefficients  $d_{\ell,m}$ ,

$$\hat{\delta}_g^{(i)}(\boldsymbol{\theta}) = \sum_{\ell,m} d_{\ell,m}^{(i)} Y_{\ell,m}(\boldsymbol{\theta}). \quad (19)$$

From the  $d_{\ell,m}$  coefficients we can measure the angular power spectrum of the estimated density field,

$$D_{ij}(\ell) = \frac{1}{2\ell+1} \sum_{m=-\ell}^{+\ell} d_{\ell,m}^{(i)} d_{\ell,m}^{(j)*}. \quad (20)$$

The measured power spectrum  $D_{ij}(\ell)$  contains contributions from both the underlying galaxy clustering signal and the Poisson noise associated with the discretised number counts in Eq. (18). Explicitly, the Poisson noise contributes to the auto-power spectra in a tomographic analysis, and the power spectrum of the Poisson noise in a tomographic bin  $i$  is given by (e.g. Loureiro et al. 2019, Nicola et al. 2020)

$$N_i(\ell) = \Omega_p \frac{\bar{w}}{\bar{n}_i^p}, \quad (21)$$

where  $\Omega_p$  is the angular size in steradians of the pixels that form the pixelised overdensity map, and  $\bar{w}$  is the average value of the mask over all pixels on the sky. For this work, we use a binary mask whereby pixels are set to 1 inside the observed footprint and 0 outside the footprint.

The Poisson noise and underlying galaxy clustering signal are uncorrelated, so the angular power spectrum of the *estimated* density field is simply the sum of the two components:

$$D_{ij}(\ell) = C_{ij}^{\delta_g \delta_g}(\ell) + N_i(\ell) \delta_{ij}. \quad (22)$$

### 3.2.3. Galaxy-galaxy lensing estimators

In order to measure the galaxy-galaxy lensing signal, we estimate the angular power spectrum from the harmonic coefficients of the density and shear fields. Since we expect that  $B_{\ell,m} = 0$ , the galaxy-galaxy lensing power spectrum is characterised by the cross-correlation of the density field and the shear  $E$ -mode,

$$\hat{C}_{ij}^{\delta_g \gamma}(\ell) = \hat{C}_{ij}^{\delta_g E}(\ell) = \frac{1}{2\ell+1} \sum_{m=-\ell}^{+\ell} d_{\ell,m}^{(i)} E_{\ell,m}^{(j)*}, \quad (23)$$

for given tomographic bins  $i, j$ .

### 3.3. Estimators on the cut sky

The above framework is defined for the case of a full sky being observed. In reality there will be partial sky coverage due to unobserved regions, or bright stars, meaning that a survey mask  $W(\boldsymbol{\theta})$  is applied to the shear and overdensity fields, which leads to mode mixing in the derived power spectra. Following the techniques of Peebles (1973), Brown et al. (2005), and Hikage et al. (2011), we summarise the expressions for these ‘pseudo’ 3×2pt signals on the cut sky below.

For a spin-0 clustering field, the partial sky overdensity  $\tilde{\delta}_g(\boldsymbol{\theta})$  is related to the full-sky field by the  $W(\boldsymbol{\theta})$  window function,

$$\tilde{\delta}_g(\boldsymbol{\theta}) = W(\boldsymbol{\theta}) \delta_g(\boldsymbol{\theta}), \quad (24)$$

and the spherical harmonic coefficients of the cut-sky field,  $\tilde{d}_{\ell,m}$  are related to the full-sky coefficients according to

$$\tilde{d}_{\ell,m} = \sum_{\ell',m'} {}_0W_{\ell\ell'}^{mm'} d_{\ell',m'}, \quad (25)$$

where  ${}_0W_{\ell\ell'}^{mm'}$  is the harmonic space window function characterised by the mask. For a general spin- $s$  field, the spin-weighted harmonic window function is given in terms of the spin-weighted  ${}_sY_{\ell,m}(\boldsymbol{\theta})$  polynomials and integrating over the full sphere:

$${}_sW_{\ell\ell'}^{mm'} = \int d\boldsymbol{\theta} {}_sY_{\ell',m'}(\boldsymbol{\theta}) W(\boldsymbol{\theta}) {}_sY_{\ell,m}^*(\boldsymbol{\theta}). \quad (26)$$

This framework can be extended to relate the observed cut-sky shear field components,  $\tilde{\gamma}_{1,2}(\boldsymbol{\theta})$ , to their full-sky counterparts,  $\gamma_{1,2}(\boldsymbol{\theta})$ , via a spin-2 harmonic decomposition,

$$\begin{aligned} \tilde{\gamma}_1(\boldsymbol{\theta}) \pm i\tilde{\gamma}_2(\boldsymbol{\theta}) &= W(\boldsymbol{\theta}) [\gamma_1(\boldsymbol{\theta}) \pm i\gamma_2(\boldsymbol{\theta})] \\ &= \sum_{\ell,m} (\tilde{E}_{\ell,m} \pm i\tilde{B}_{\ell,m}) {}_{\pm 2}Y_{\ell,m}(\boldsymbol{\theta}). \end{aligned} \quad (27)$$

Following Lewis et al. (2001), the cut sky harmonic coefficients  $(\tilde{E}_{\ell,m}, \tilde{B}_{\ell,m})$  are related to the spin-weighted harmonic window functions according to:

$$\tilde{E}_{\ell,m} = \sum_{\ell',m'} (E_{\ell',m'}^+ W_{\ell\ell'}^{+mm'} + B_{\ell',m'}^- W_{\ell\ell'}^{-mm'}), \quad (28)$$

$$\tilde{B}_{\ell,m} = \sum_{\ell',m'} (B_{\ell',m'}^+ W_{\ell\ell'}^{+mm'} - E_{\ell',m'}^- W_{\ell\ell'}^{-mm'}), \quad (29)$$

where we have defined the compound matrices,

$$W_{\ell\ell'}^{+mm'} = \frac{1}{2} ({}_2W_{\ell\ell'}^{+mm'} + {}_{-2}W_{\ell\ell'}^{+mm'}), \quad (30)$$

$$W_{\ell\ell'}^{-mm'} = \frac{i}{2} ({}_2W_{\ell\ell'}^{-mm'} - {}_{-2}W_{\ell\ell'}^{-mm'}), \quad (31)$$

and where Eq. (26) is evaluated for  $s = \pm 2$ .

Finally, the measured cut-sky power spectra elements,  $\tilde{C}_\ell$ , can be related to the true underlying full-sky elements,  $C_\ell$ , by the mixing matrix  $M_{\ell\ell'}$  (see the Appendix in Brown et al. 2005 for a full derivation), which contains the coupled harmonic space information about the survey mask. Here,  $C_\ell$  denotes the elements of a column vector representing  $C(\ell)$  evaluated at integer  $\ell$ , which we will adopt as a shorthand description of the power spectrum for the remainder of this work. Taking the expectation value, we then find

$$\langle \tilde{C}_\ell^{(i,j)} \rangle = \sum_{\ell'} M_{\ell\ell'}^{(i,j)} C_{\ell'}^{(i,j)}, \quad (32)$$

where we have introduced the tomographic dependence of the power spectra and window functions as the superscripts  $(i, j)$ .

For our analysis, we work with the Pseudo- $C_\ell$  power spectrum of the signal measured directly from the catalogue data,  $\tilde{S}_\ell$ . The expected value for this measured signal is calculated as the sum of the cosmological signal on the masked sky and the noise

$$\begin{aligned} \langle \tilde{S}_\ell^{(i,j)} \rangle &= \langle \tilde{C}_\ell^{(i,j)} \rangle + \langle N_\ell^{(i,j)} \rangle \\ &= \left( \sum_{\ell'} M_{\ell\ell'}^{(i,j)} C_{\ell'}^{(i,j)} \right) + \langle N_\ell^{(i,j)} \rangle. \end{aligned} \quad (33)$$

Here, the noise term  $N_\ell^{(i,j)}$  arises due to shape noise for the cosmic shear field and Poisson noise for the galaxy clustering field, and is only non-zero for the auto-power spectra. Explicitly, for each  $3 \times 2$ pt component, the cut-sky Pseudo- $C_\ell$  power spectra are given by the following expressions.

- Angular clustering

$$\langle \tilde{C}_\ell^{\delta_g(i)\delta_g(j)} \rangle = \sum_{\ell'} W_{\ell\ell'}^{00}(i,j) C_{\ell'}^{\delta_g(i)\delta_g(j)}. \quad (34)$$

- Cosmic shear

$$\begin{aligned} \left( \begin{array}{c} \tilde{C}_\ell^{E(i)E(j)} \\ \tilde{C}_\ell^{E(i)B(j)} \\ \tilde{C}_\ell^{B(i)B(j)} \end{array} \right) &= \sum_{\ell'} \left[ \begin{array}{ccc} W_{\ell\ell'}^{++}(i,j) & W_{\ell\ell'}^{+-}(i,j) + W_{\ell\ell'}^{-+}(i,j) & W_{\ell\ell'}^{--}(i,j) \\ -W_{\ell\ell'}^{+-}(i,j) & W_{\ell\ell'}^{++}(i,j) - W_{\ell\ell'}^{-+}(i,j) & W_{\ell\ell'}^{--}(i,j) \\ W_{\ell\ell'}^{-+}(i,j) & -W_{\ell\ell'}^{+-}(i,j) - W_{\ell\ell'}^{-+}(i,j) & W_{\ell\ell'}^{--}(i,j) \end{array} \right] \\ &\quad \left( \begin{array}{c} C_{\ell'}^{E(i)E(j)} \\ C_{\ell'}^{E(i)B(j)} \\ C_{\ell'}^{B(i)B(j)} \end{array} \right). \end{aligned} \quad (35)$$

- Galaxy-galaxy lensing

$$\left( \begin{array}{c} \tilde{C}_\ell^{\delta_g(i)E(j)} \\ \tilde{C}_\ell^{\delta_g(i)B(j)} \end{array} \right) = \sum_{\ell'} \left( \begin{array}{cc} W_{\ell\ell'}^{0+}(i,j) & W_{\ell\ell'}^{0-}(i,j) \\ -W_{\ell\ell'}^{0-}(i,j) & W_{\ell\ell'}^{0+}(i,j) \end{array} \right) \left( \begin{array}{c} C_{\ell'}^{\delta_g(i)E(j)} \\ C_{\ell'}^{\delta_g(i)B(j)} \end{array} \right). \quad (36)$$

Here, we have defined the tomographic mixing functions,

$$W_{\ell\ell'}^{MN}(i,j) = \frac{1}{2\ell+1} \sum_{mm'} W_{\ell\ell'mm'}^{M,i} (W_{\ell\ell'mm'}^{N,j})^*, \quad (37)$$

for  $M, N = (0, +, -)$ ; the  $W_{\ell\ell'mm'}^{+/-}$  are as defined in Eq. (31) and  $W_{\ell\ell'mm'}^0 = {}_0W_{\ell\ell'mm'}^{mm'}$  from Eq. (25).

### 3.4. Bandpowers

Following the technique of Hivon et al. (2002), it is often convenient to bin the Pseudo- $C_\ell$  measured on the cut sky in  $\ell$  space. This gives a reduction in the errors on the power spectrum estimator and allows the mixing matrix (Eq. 32) to remain invertible in the case of large and complex sky cuts. For a set of bins, denoted by the index  $b$ , with bin boundaries  $\{\ell_{\text{low}}^b < \ell_{\text{high}}^b < \ell_{\text{low}}^{b+1} < \ell_{\text{high}}^{b+1} < \dots\}$  we take a binning operator  $P_{b\ell}$  defined as

$$P_{b\ell} = \begin{cases} \frac{1}{2\pi} \frac{\ell(\ell+1)}{\ell_{\text{low}}^{b+1} - \ell_{\text{low}}^b}, & \text{if } 2 \leq \ell_{\text{low}}^b \leq \ell < \ell_{\text{low}}^{b+1} \\ 0, & \text{otherwise.} \end{cases} \quad (38)$$

The elements of the binned Pseudo- $C_\ell$  power spectrum are termed ‘bandpowers’ and are calculated as

$$\tilde{C}_b = \sum_{\ell} P_{b\ell} \tilde{C}_\ell. \quad (39)$$

We note that our approach to estimate angular power spectra is similar to the analysis that is expected to be applied to the *Euclid* DR1 sample (Euclid Collaboration: Tessore et al. 2024).

## 4. Methods: simulating mock catalogues

In this section, we describe the modelling process and present the simulation pipeline with which we construct Stage IV-like mock cosmic shear catalogues. Our code for this simulation, SWEPT (Simulator for WEak lensing Power spectrum Tomography), is found at <https://github.com/j-hw-wong/SWEPT>.

For a given fiducial cosmology and background galaxy redshift distribution, we firstly generate a theoretical prediction for the full-sky  $3 \times 2$ pt power spectra  $[C_{ij}^{\gamma\gamma}(\ell), C_{ij}^{\delta_g \delta_g}(\ell), C_{ij}^{\delta_g \gamma}(\ell)]$  at multiple, finely-spaced redshift intervals. From the  $3 \times 2$ pt data vectors, we generate a realisation on the sky of the galaxy clustering,  $\delta_g(\boldsymbol{\theta})$ , and shear  $[\gamma_1(\boldsymbol{\theta}), \gamma_2(\boldsymbol{\theta})]$  fields at each point in redshift space covered by our chosen galaxy sample. In this way, we approximate the full 3D cosmological information with a set of 2D sky maps that represents the behaviour of the  $3 \times 2$ pt observable fields as the background Universe evolves over time and redshift.

Finally, we perform a random sampling routine and Poisson sample the galaxy clustering fields at each redshift to populate the sky with galaxies that trace the underlying matter distribution. We construct a mock catalogue by then assigning the weak lensing observables  $[\kappa(\boldsymbol{\theta}), \gamma_1(\boldsymbol{\theta}), \gamma_2(\boldsymbol{\theta})]$  from the field values of the cosmic shear maps at the positions of each pixel hosting a galaxy.

This simulation pipeline consists of a number of distinct stages of calculation that are executed in series. We describe each step in detail below. In Fig. 1 we present a flowchart diagram showing the workflow of our simulation to produce the final mock catalogues.

### 4.1. Generation of $n(z)$ redshift sample

The first step is the construction of a galaxy population that follows a given  $n(z)$  redshift distribution. Following Sipp et al. (2021), we take a redshift probability distribution  $p(z)$  typical of a Stage IV survey that has the functional form,

$$p(z) \propto \left( \frac{z}{z_0} \right)^2 \exp \left[ - \left( \frac{z}{z_0} \right)^{1.5} \right], \quad (40)$$

where  $z_0$  is the characteristic redshift constant chosen such that the median redshift of the sample satisfies  $z_{\text{median}} = \sqrt{2} z_0$ . We expect that this chosen form for  $p(z)$  will be a good approximation for the *Euclid* DR1 galaxy sample. We note that the measured cosmological constraints would change if the real galaxy distribution is observed to be significantly different.

Following the definition of the redshift probability distribution, we then set the simulated redshift range  $[z_{\min}, z_{\max}]$  and a precision  $dz$  to which galaxy redshifts are generated. A raw galaxy sample  $n(z)$  is then created by performing a sampling routine to draw a chosen total number of galaxies  $N_{\text{gal}}$  that traces the  $p(z)$  redshift probability distribution.

We highlight that the functional form for  $p(z)$ , the total observed galaxy density  $N_{\text{gal}}$ , and the redshift range and precision  $[z_{\min}, z_{\max}, dz]$  are left as free choices in our simulation that can arbitrarily be changed to match the specifications of a chosen survey.

#### 4.2. Calculation of theoretical 3×2pt data vector for each galaxy redshift

Following the simulation of a galaxy population  $n(z)$ , we aim to generate 2D realisations on the sky of the galaxy clustering and weak lensing fields for each redshift that we sample galaxies at. To do this, we first need a prediction for the 3×2pt power spectra at each redshift. This set of power spectra is constructed by converting the raw  $n(z)$  sample into a ‘binned’ population and creating a table where every column contains the galaxy number count at each specific, discrete redshift that has been sampled in the  $p(z)$ .

This process allows us to retain the correlations in the 3×2pt fields between the different, finely-spaced redshift slices. In Fig. 2 we show the *Euclid* DR1-like redshift distribution we consider for our work and demonstrate the effects of binning and normalising the population. This ultimately allows us to generate a set of 2D slices of the 3×2pt signal that approximates the full 3D cosmological information.

In addition to the ‘binned’  $n(z)$ , we require a matter power spectrum  $P_{\delta}(k)$ , which consists of both a linear and nonlinear component, and a galaxy bias model  $b(k, z)$  which represents the scale- and redshift-dependent relation between the distribution of galaxies and the underlying matter field that they trace. On large scales ( $\sim 30 h^{-1}$  Mpc) this relation is found to be well approximated with a linear model (Verde et al. 2002) and for the purposes of this work we assume that the galaxy bias takes the form of a constant,  $b$ . While it is beyond the scope of this work, we note that our framework has the flexibility to incorporate both scale- and redshift-dependent bias models, and the effects of these choices could be investigated in a future study.

To construct the final theoretical 3×2pt power spectra at each redshift, we use CosmoSIS (Zuntz et al. 2015), a parameter estimation code which specialises in the joint modelling of cosmological power spectra and exploration of parameter constraints for cosmic shear and galaxy clustering studies. Explicitly, we run a CosmoSIS pipeline which executes the following modules.

- CAMB (Code for Anisotropies in the Microwave Background, Lewis et al. 2000), used to model the linear matter power spectrum, which describes the evolution of density perturbations in the early Universe.
- `halofit_takahashi` (Smith et al. 2003, Takahashi et al. 2012), used to model the matter power spectrum in the non-linear regime by scaling the linear component using fitting functions derived from simulations.
- `constant_bias`, used to define the functional form of the galaxy bias for modelling the galaxy clustering and galaxy-galaxy lensing signals. We make the assumption that, on the large scales which we focus on for this work, the galaxy bias can be sufficiently described using a constant.

- `load_nz`, used to process and normalise the ‘binned’  $n(z)$  galaxy population based on the user-defined redshift boundaries of each column. The resulting  $n(z)$  table products can then be used to generate the 3×2pt signal.
- `project_2d`, used for calculation of the theoretical 3×2pt data vector by evaluating the Limber approximation to project the 3D line-of-sight information into 2D angular power spectra.

For the background cosmology in the CosmoSIS pipeline and our overall simulation, we work with a flat  $w_0 w_a$  Universe with  $\Omega_m = 0.3$  and  $H_0 = 70 \text{ km s}^{-1} \text{ Mpc}^{-1}$ . For the matter power spectrum generated using the CAMB module in CosmoSIS, we take the latest best fit *Planck* values (see Planck Collaboration: Aghanim et al. 2020 and references therein):

- optical depth to reionisation,  $\tau = 0.05$ ;
- scalar spectral index,  $n_s = 0.96$ ;
- primordial amplitude of power,  $A_s = 2.1 \times 10^9$ .

For the constant galaxy bias model, we choose a value  $b = 0.4$ , which is chosen to avoid numerical issues encountered when generating the shear and clustering fields on the sky (see Sect. 4.4 for a further discussion of this point).

Lastly, we choose to work with the fiducial values  $(w_0, w_a) = (-1, 0)$ . However, we emphasise that these values are free global parameters that can arbitrarily be changed in our simulation pipeline. While it is beyond the scope of this work, future studies could explore how the final conclusions presented here may change based on the fiducial  $(w_0, w_a)$  choices.

#### 4.3. Generation of weak lensing and clustering maps

In order to simulate the cosmological 3×2pt signal on the sky, we next generate a set of full-sky maps of the observables contained in the 3×2pt power spectra calculated at each redshift sampled from the  $n(z)$  distribution.

For the galaxy clustering component, we require the observed galaxy overdensity field  $\delta_g(\theta)$ , a scalar quantity, while for weak lensing there are three observable quantities on the sky: the scalar convergence field  $\kappa(\theta)$  describing the lensing-induced magnification of a source, and the components of the spin-2 shear field,  $\gamma_1(\theta)$  and  $\gamma_2(\theta)$ .

These fields are generated on the sky using HEALPix (Górski et al. 2005), a pixelisation technique which offers the ability to represent data on the sphere. In order to generate the pixelised maps from the 3×2pt data vector, we use the Full-sky Lognormal Astro-fields Simulation Kit (FLASK; Xavier et al. 2016) which creates realisations of an arbitrary set of correlated fields on the sky from their given tomographic power spectra via Cholesky decomposition.

While FLASK has the capacity to generate both lognormal and Gaussian-distributed realisations of the chosen fields, for the purposes of this work we choose to consider only Gaussian fields, on the premise that complete information of a Gaussian field is directly captured in the power spectrum.

#### 4.4. Construction of mock catalogue

The FLASK routine yields a 2D HEALPix map of the galaxy clustering, convergence and cosmic shear fields at each redshift  $z_s$  that is sampled in the  $p(z)$  distribution.

In order to construct a mock catalogue, we first place galaxies at angular positions on the sky by Poisson-sampling the

galaxy density field  $\delta_g^{z_s}(\boldsymbol{\theta})$  at each redshift  $z_s$ . We convert this into an observed galaxy population by Poisson-sampling the cell value to generate a pixelised integer number count of galaxies on the sky at the redshift slice  $z_s$ ,

$$n_{\text{gal}}^{z_s}(\boldsymbol{\theta}) = \text{Poisson} \left\{ \bar{n}_{\text{gal}}^{z_s}(\boldsymbol{\theta}) [1 + \delta_g^{z_s}(\boldsymbol{\theta})] \right\}, \quad (41)$$

where  $\bar{n}_{\text{gal}}^{z_s}(\boldsymbol{\theta})$  is the average number of galaxies per pixel on the sky at redshift  $z_s$ , which is defined from the sampled galaxy distribution  $n(z)$  in Eq. (40).

In order to execute Poisson-sampling of the density field, the minimum value of the field must satisfy  $\delta_g(\boldsymbol{\theta}) \geq -1$ . Due to the nature of Gaussian realisations on the sky, there can be random pixels generated that have the unphysical value  $\delta_g < -1$ . To reduce the impact of this effect, we take a redshift-independent galaxy bias value of  $b = 0.4$ , which reduces the frequency of these random occurrences. We note that such values of  $b < 1$ , while less realistic, are a choice taken by other studies in the literature (e.g. Tessore et al. 2023) that have investigated Gaussian realisations of the  $3 \times 2$ pt fields on the sky. Quantitatively, we expect that to first order this choice will not affect the cosmic shear measurements, since the bias term does not feature in the weak lensing kernel (Eqs. 1, 2). For the angular clustering and galaxy-galaxy lensing signals, the bias term acts to scale the amplitude of the power spectrum. Since we use a constant bias over all angular scales and redshift, we expect that the choice of  $b$  would change the absolute values of constraints on  $(w_0, w_a)$  measured from our simulations, but would not alter the relative measurements that compare the constraints between different tomographic binning schemes.

In addition, we reject the redshift range  $z < 0.3$  in which the evolution of galaxy clustering is more likely to produce such unphysical pixels. However, we note that at this redshift range there is also the least amount of information contained in the cosmic shear signal, since there is comparatively little foreground structure to induce the weak lensing effect.

We assign an angular (RA, Dec) position to each galaxy by placing them at the centre of the pixel they are Poisson-sampled in. The final galaxy ‘observation’ to create a mock shear catalogue is then a straightforward assignment process. Each galaxy is described with a data vector of its (RA, Dec,  $z$ ) values. We then append to this observed data the value of the cosmic shear  $[\kappa(\boldsymbol{\theta}), \gamma_1(\boldsymbol{\theta}), \gamma_2(\boldsymbol{\theta})]$  fields at the specific sky position and redshift that the galaxy is found at.

By repeating this procedure for each galaxy in our sampled population, we produce a final cosmic shear catalogue which

- consists of a galaxy population that traces a survey-specified number density and predicted redshift probability distribution  $p(z)$ ;
- statistically represents on the sky the information contained in the theoretical  $3 \times 2$ pt power spectra calculated from a chosen underlying cosmology.

#### 4.5. Pipeline overview

The overall workflow of our pipeline is presented in Fig. 1. Our simulation-based approach offers an approximate, but rapid technique for exploring the impact of different analysis choices on the precision of cosmological constraints that can be achieved with *Euclid*. While a full  $N$ -body simulation to create a catalogue would provide the most complete astrophysical information, it is extremely computationally costly to generate and would typically yield only a few realisations. Correspondingly, introducing

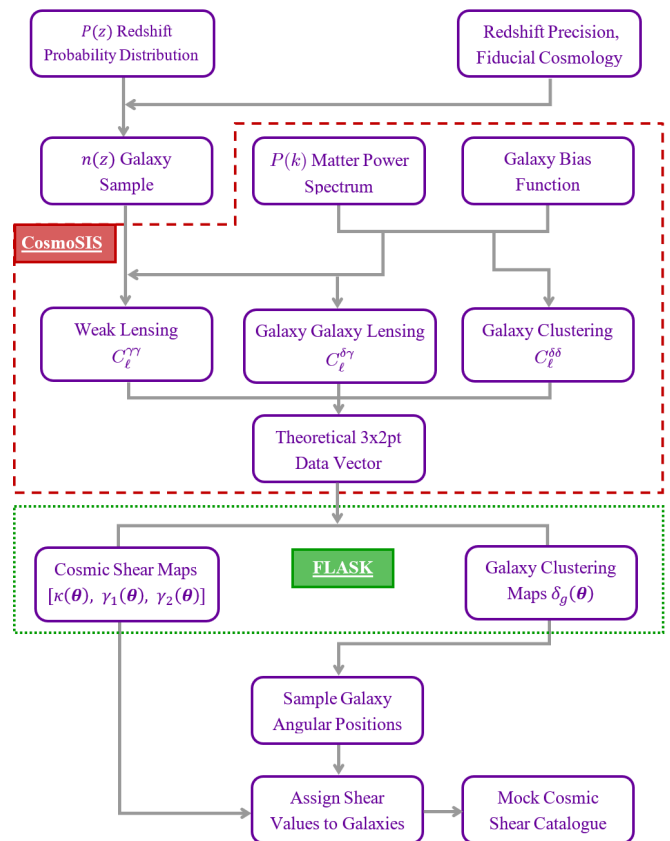


**Fig. 1.** A flowchart describing the structure of our simulation to generate Stage IV-like mock galaxy catalogues from 2D realisations on the sky of the  $3 \times 2$ pt signal that traces an underlying redshift distribution and fiducial cosmology. The red dashed and green dotted sections represent the simulation stages that are executed using CosmoSIS and FLASK respectively.

or removing any additional astrophysical or observational features in the simulation to test their impact on observables and cosmological measurements would be complex and inefficient.

As discussed in Sect. 2, previous studies on the choice of  $3 \times 2$ pt tomography have typically focused only on exploring a predefined signal, without generating a mock observation on the sky. Our method offers an alternative to such approaches. Since we replicate a real analysis by measuring the  $3 \times 2$ pt signal from the simulated data, this equips us with a unique capability to introduce complex observational and astrophysical effects at the catalogue level, and rapidly explore their effects on measurements of cosmological parameters. We note that by using the map-based simulation approach, we can practically generate and work with many realisations of the Universe to further improve the statistical power of the analysis.

#### 4.6. Simulated noise and errors

The basic execution of our pipeline contains intrinsic Poisson noise in the galaxy clustering signal, which has the noise power spectrum given in Eqs. (21, 22). In addition to the Poisson noise, we can also increase the realism of our simulation by introducing redshift uncertainties and shape noise in the galaxies, which are included as an optional feature in our simulation.



#### 4.6.1. Redshift uncertainties

For a realistic survey, we require either spectroscopic or photometric analysis of individual galaxies in order to measure their redshift. While the spectroscopic measurement offers a very precise estimate of the galaxy’s true redshift, it is unfeasible to yield a spectroscopic redshift for every galaxy in a survey. Comparatively, there are much larger uncertainties when deriving redshifts via the photometric method, which relies on fitting the galaxy’s observed spectral energy distribution (see e.g. [Euclid Collaboration: Ibert et al. 2021](#) for an overview of redshift measurement techniques for *Euclid*).

When constructing the final survey catalogues in our pipeline (Sect. 4.4) we can optionally introduce uncertainty in the galaxy redshifts associated with such measurement techniques. Explicitly, we expect that, to first order, the photometric uncertainty on a measured redshift will be Gaussian-distributed with standard deviation  $\sigma_z$  dependent on the redshift,

$$\sigma_z = \sigma_z^{\text{phot}}(1 + z), \quad (42)$$

where  $\sigma_z^{\text{phot}}$  is a constant. In order to introduce this effect into our pipeline, for each galaxy at redshift  $z$ , we convert the ‘true’ redshift of the galaxy in the catalogue to a ‘measured’ redshift by drawing an estimated value from a Gaussian distribution with standard deviation  $\sigma_z$  and mean  $z$ .

In addition to the Gaussian-distributed uncertainty in the photo- $z$ s, there will be some catastrophic outliers due to limitations in the photometric fitting procedure. Explicitly, the measured SED of the galaxy can be fit to a specific template (see e.g. [Euclid Collaboration: Desprez et al. 2020](#) for an overview). However, confusion between given pairs of spectral lines can lead to a measured galaxy redshift that is catastrophically inaccurate. In the technique of [Jouvel et al. \(2011\)](#), we can model a ‘catastrophic’ redshift estimate using the expression

$$z_{\text{cata}} = (1 + z) \frac{\lambda_{\text{break-rf}}}{\lambda_{\text{break-cata}}}, \quad (43)$$

where  $\lambda_{\text{break-rf}}$  is the true rest-frame wavelength of a break feature in an SED model, and  $\lambda_{\text{break-cata}}$  is the wavelength of the break feature that is predicted in the fitting procedure. As a first-order approximation, in the redshift range  $z \leq 2.5$ , [Jouvel et al. \(2011\)](#) suggest that the Lyman- $\alpha$  line, Lyman-break, Balmer-break and 4000-Å break (D4000), and permutations between pairs of these four features, will contribute to the catastrophic redshift estimation.

Within our simulation, we include the option to model this effect by converting the true redshifts of a chosen percentage of the galaxy population into a catastrophic measurement based on a given set of spectral line pairs.

#### 4.6.2. Shape noise

A further significant source of noise in a weak lensing analysis is the shape noise. Galaxies have an intrinsic ellipticity  $\epsilon^{\text{int}}$  which acts as an irreducible source of confusion when estimating the weak lensing-induced shape distortion  $\gamma$ . Under the assumption that galaxies have no preferred ellipticity on average, one can model the shape noise to be Gaussian-distributed with standard deviation  $\sigma(\epsilon^{\text{int}})$ .

We introduce this as an optional effect in our simulation by drawing shape noise error quantities from a Gaussian distribution with standard deviation  $\sigma(\epsilon^{\text{int}})$ . This error is then attributed

to each galaxy by adding the component  $\sigma(\epsilon^{\text{int}})/\sqrt{2}$  to each of the  $\gamma_1(\theta)$  and  $\gamma_2(\theta)$  galaxy observable values in the catalogue.

Finally, when measuring tomographic shear power spectra from the catalogues, we model the uncertainty due to this shape noise by using the following expression for the shape noise contribution to the  $E$ -mode power spectrum on the cut sky,

$$\tilde{N}_\ell^{ij} = \frac{(\sigma_\epsilon/\sqrt{2})^2}{\bar{N}_i} \delta_{ij}, \quad (44)$$

where,  $\bar{N}_i$  is the Poisson noise associated with the tomographic bin  $i$  (Eq. 21), and  $\delta_{ij}$  is the Kronecker delta – i.e. the shape noise only contributes to auto-correlation power spectra.

## 5. Inference routine

### 5.1. Grid-based Gaussian likelihood

The central aim of this work is to explore the 3×2pt signal for different tomographic configurations, and identify the optimum tomographic binning strategy that provides the best constraints for the time evolving dark energy equation of state. In order to derive parameter constraints, we perform a grid based inference routine using a Gaussian likelihood in which we vary the  $(w_0, w_a)$  parameters in a  $w_0w_a$ CDM cosmology (see Sect. 1) while all other cosmological parameters are held at the fixed fiducial values presented in Sect. 4.2. An in-depth discussion on the validity of the Gaussian likelihood and the description of the grid-based framework adopted is given in [Upham et al. \(2021\)](#). Explicitly, the multivariate Gaussian likelihood is given by

$$\mathcal{L} = \frac{1}{(2\pi)^{k/2} |\mathbf{C}|^{1/2}} \exp\left[-(\mathbf{D} - \mathbf{M})^T \mathbf{C}^{-1} (\mathbf{D} - \mathbf{M})\right], \quad (45)$$

where  $\mathbf{D}$  is the (mock) observed data vector of length  $k$ ,  $\mathbf{M}$  is a given theory data vector, and  $\mathbf{C}$  is the covariance matrix for the data vector  $\mathbf{D}$ . The 2-dimensional posterior distribution,  $p(\theta | \mathbf{D})$ , of the model parameters  $\theta$  is then given by Bayes’ theorem,

$$p(\theta | \mathbf{D}) \propto \pi(\theta) \mathcal{L}(\mathbf{D} | \theta), \quad (46)$$

where  $\mathcal{L}(\mathbf{D} | \theta)$  is the likelihood and  $\pi(\theta)$  is the prior knowledge. For this work, we assume a flat prior in  $(w_0, w_a)$ .

### 5.2. Numerical covariance matrix

A key ingredient of the Bayesian method is the covariance matrix  $\mathbf{C}$ . For our work, we use a numerical covariance matrix in which we estimate the errors using a large number of realisations. After measuring the bandpowers of the 3×2pt Pseudo- $C_\ell$  data vector,  $\tilde{C}_b$  (Eq. 39) for each realisation, the elements of the covariance matrix are then constructed from the scatter of the realisations with respect to the mean,

$$C_{bb'} = \left\langle (\tilde{C}_b - \tilde{C}_{b,av})(\tilde{C}_{b'} - \tilde{C}_{b',av}) \right\rangle, \quad (47)$$

where  $\tilde{C}_{b,av}$  is the mean recovered bandpower in band,  $b$ , and the angled brackets denote an average over all realisations.  $C_{bb'}$  are the elements of the covariance matrix  $\mathbf{C}$ .

While the numerical covariance matrix provides an estimate of the true errors intrinsic in our simulation method, it will also

contain ‘shot noise’ due to the finite number of simulations used. By definition, a greater number of simulations leads to more suppression of this shot noise, until the limit of infinite realisations where the shot noise will average to zero and leave only the true signal in the covariance matrix.

One complexity of the tomographic approach is that as a greater number of redshift bins is used for the  $3\times 2$ pt analysis, the data vector becomes larger. Therefore, more simulations are needed to suppress the shot noise such that it does not dominate over the true signal and lead to inaccurate posterior constraints. For exploring configurations with  $> 10$  tomographic bins, we find that, at an optimistic minimum,  $> 10^4$  simulations would be needed in order for the random noise to be suppressed to a suitable level below the true signal. Since this number of realisations is impractical to generate, we work with a smaller number of realisations and introduce a filtering approach to remove the random noise in the covariance matrix.

By exploring the elements of the numerical covariance matrix as a function of number of realisations, we find that the signal is dominated by the diagonals of each ‘block’. The off-diagonal terms, at several orders of magnitude lower, are dominated by homogeneous noise. After setting the off-diagonal elements of each block to zero, we find that this filtering approach allows us to work with a practical number of realisations (400). We note that this procedure will remove true covariance from the off-diagonal elements. In Appendix B, we quantitatively explore the effects of this filtering. In particular, we derive ‘correction factors’ with which we can adjust our measured posterior areas to estimate the ‘true’ area that could be achieved in the limit of an infinite number of realisations. We have confirmed that our final conclusions on the optimum  $3\times 2$ pt tomographic binning approach do not change regardless of whether one chooses to apply these correction factors.

## 6. Impact of tomography on dark energy constraints

We now present constraints on the  $(w_0, w_a)$  parameters measured from 400 realisations of our simulated  $3\times 2$ pt catalogue data using the inference method described in Sect. 5, for a range of different tomographic binning configurations. For a *Euclid*-like survey, we take a sample of  $3 \times 10^8$  galaxies drawn in the range  $0.3 \leq z < 2.7$  from the  $p(z)$  defined in Eq. (40) using the constant  $z_0 = 0.636$  to yield a sample with a median redshift  $z_{\text{med}} = 0.9$ , matching that predicted for *Euclid* (Laureijs et al. 2011). We place these galaxies within an approximation of the *Euclid* DR1 footprint ( $\sim 2600 \text{ deg}^2$ , presented in Fig. 2) to achieve the target galaxy number density,  $30 \text{ gal/arcmin}^2$ , on the sky. We use these survey characteristics for all results presented in this work.

For generating the  $3\times 2$ pt fields on the sky, we use a HEALPix grid with resolution  $N_{\text{side}} = 1024$ . This allows us to generate catalogues from power spectra that are evaluated up to angular scales of  $\ell = 2000$ . Figure 2 shows the  $n(z)$  model that we use alongside examples of the generated  $3\times 2$ pt fields and the approximate *Euclid* DR1 mask that we use.

We sample galaxies to a redshift resolution  $dz = 0.1$ , which we note is slightly more pessimistic than the target accuracy for the *Euclid* photo- $z$  estimation for weak lensing science,  $\sigma_z/(1+z) \leq 0.05$ . However, due to our simulation methodology, we find that this is the limiting precision that allows for a consistent recovery of the fiducial cosmology from the 2-point statistics measured from the catalogues. In Appendix A we present our validation methodology to investigate the accuracy of our simulation method and demonstrate the ability of our pipeline

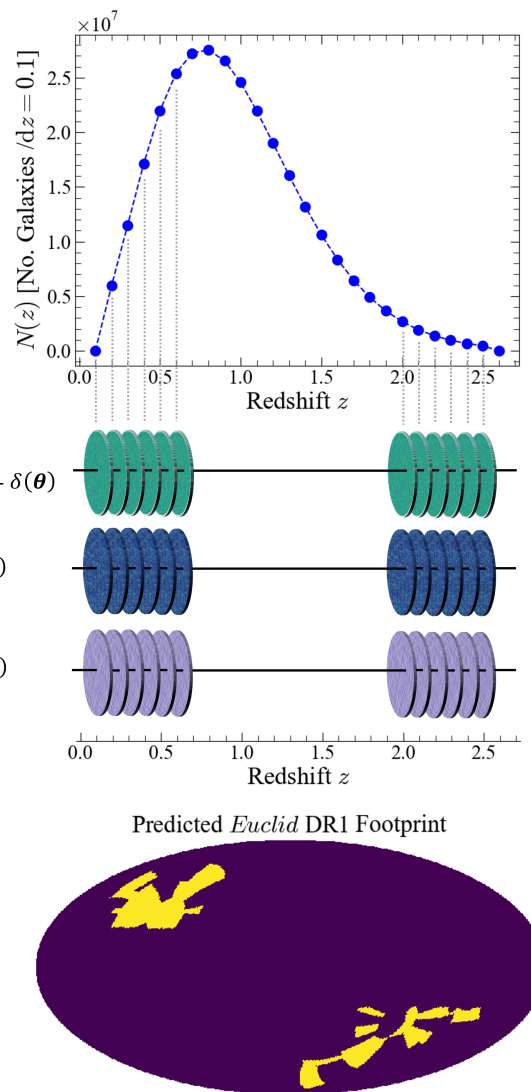


**Fig. 2.** Illustration of the method used to simulate a mock weak lensing survey. 2D maps of the correlated  $3\times 2$ pt fields are generated at finely-sampled points in redshift. These 2D maps are used to approximate the full 3D cosmological information of the  $3\times 2$ pt signal. From the overdensity fields, we Poisson sample a galaxy population that traces the underlying  $n(z)$  distribution. We then assign the correlated weak lensing observables to each galaxy from the shear field values at the galaxy’s angular position on the sky at a given redshift. We show an early approximation of the *Euclid* DR1 footprint at the bottom of the figure which we have used to create our *Euclid*-like simulations. The ‘observed’ region is shown in yellow. (The actual *Euclid* DR1 footprint will be significantly different to that shown here.)

to self-consistently reproduce the underlying  $3\times 2$ pt signal predicted by the input cosmology.

Following Sect. 3.2 we measure the  $3\times 2$ pt Pseudo- $C_\ell$  bandpowers of the data in the catalogues to derive tomographic constraints on dark energy, meaning that the theoretical model for the full sky power spectra needs to be convolved with the mixing matrices associated with the DR1 mask. In addition, a model for the noise components (see Eq. 33) is required for a direct comparison. We measure the power spectra in the multipole range  $100 \leq \ell \leq 1500$  and use 10 bandpowers binned logarithmically in angular scale. In Appendix B we discuss the impact on the  $(w_0, w_a)$  constraints resulting from the use of the finite number of 400 realisations.

By fixing all other parameters in the likelihood analysis, we find that the inference process is extremely finely tuned, and even a  $\ll 1\%$  systematic effect in the 3×2pt bandpowers (see also Appendix A.1 & Appendix A.2) leads to a biased recovery of the fiducial parameter values,  $(w_0, w_a) = (-1, 0)$ . Hence, in order to examine the effects of tomographic binning on the true cosmology, we choose to work with the fiducial data vector but use a numerical covariance matrix, which we derive from our simulated measurements (see Sect. 5.2). This ensures that we will be probing the fluctuations about the true cosmology, but we do not expect that the size of the errorbars and the  $(w_0, w_a)$  contours will change, since we retain the realistic simulated noise that is observed in the 3×2pt data from our catalogues.

To evaluate the performance of a given tomographic binning configuration, we plot the areas enclosed within the 2D  $(w_0, w_a)$  posterior contours as a function of the number of tomographic bins used. We consider three binning cases: bins equipopulated with galaxies; bins equally spaced in redshift; and bins equally spaced in fiducial comoving distance. We consider constraints for both the ‘no-noise’ simulation and the ‘realistic’ setup including Gaussian shape noise and Gaussian photo- $z$  estimation uncertainty. For the ‘noisy’ simulation, we consider an intrinsic shape noise in the source galaxies that is described by a Gaussian parameterised by a constant  $\sigma(\epsilon^{\text{int}}) = 0.3$  (e.g. [Euclid Collaboration: Paykari et al. 2020](#)) and inject this uncertainty into the shear field values assigned to each galaxy in the catalogue using the method described in Sect. 4.6.2.

To model the photo- $z$  uncertainty, we use Gaussian distributed errors with the redshift dependent deviation discussed in Sect. 4.6.1, where we take the constant  $\sigma_z^{\text{phot}} = 0.05$  to match the target uncertainty for the *Euclid* analysis as defined in [Laureijs et al. \(2011\)](#). While we model such uncertainties in the redshift and galaxy shapes, in this section we consider only unbiased redshift and shear estimates, which we note would need to be controlled in a precision 3×2pt analysis. While a comprehensive study of these issues is beyond the scope of this work, in Sect. 7 we consider the effects of contamination by catastrophic redshift errors.

For both the no-noise and noisy cases, we investigate: a 1×2pt cosmic shear only; a 1×2pt angular clustering only; and lastly a full 3×2pt analysis. For the noisy simulation measurements, we additionally plot the 1 and 2 $\sigma$  posterior contours in the  $(w_0, w_a)$  plane for a selection of equipopulated binning constraints, which we find are similar in shape to the equivalent contours in the no-noise measurements.

## 6.1. Signal-only simulations

### 6.1.1. 1×2pt cosmic shear only analysis, no-noise simulation

For a catalogue simulation in the absence of shape noise and photo- $z$  uncertainty, we measure the tomographic Pseudo- $C_\ell$  power spectra of the cosmic shear signal only, and plot in Fig. 3 the area enclosed in the  $(w_0, w_a)$  plane by the 1 and 2 $\sigma$  contours as a function of the number of redshift bins used for the analysis. We present these results for the three binning choices: equipopulated (solid line); equal redshift width (dotted line); and bins equally spaced in fiducial comoving distance (dashed line).

We find that comparatively, the equal redshift width bins cover the smallest area in  $(w_0, w_a)$  for a given number of redshift bins, indicating that this binning choice would yield the optimum constraints on the dark energy equation of state. We note that for the particular case of a single bin the shear signal is

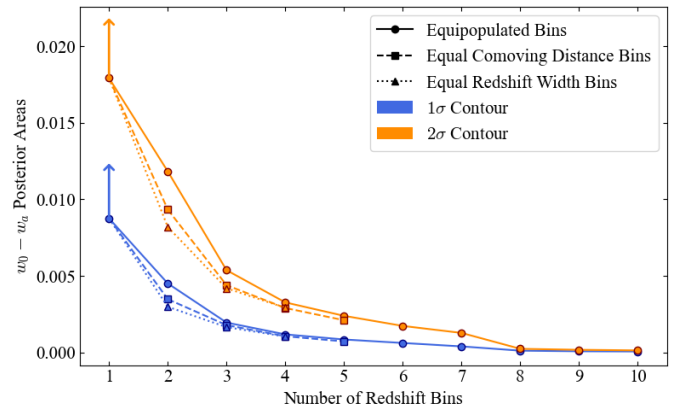


**Fig. 3.** The areas enclosed by the 1 $\sigma$  (Blue) and 2 $\sigma$  contours in the  $(w_0, w_a)$  plane, for different numbers of redshift bins used in a tomographic analysis of the cosmic shear signal measured from 400 realisations of our simulation. We show in circular markers joined with solid lines the areas measured for the equipopulated binning choice; in square markers joined with dashed lines the equal comoving distance bins; and in triangular markers joined with dotted lines the equal redshift width binning choice. Since the cosmic shear component alone is relatively weakly constraining, the 1 bin measurement does not yield a closed contour in  $(w_0, w_a)$  within the ranges of the parameter grid. Hence, the data point for this case represents a lower bound of the true value, which we represent by using a vertical arrow.

only weakly constraining and does not enclose a 2 $\sigma$  area within the prior boundaries of the parameter space. However, increasing the analysis to include just 2 bins provides sufficient constraining power to yield closed contours and place constraints on the dark energy parameters.

For a 2-bin analysis, the difference in the contour area between each choice is at a considerable level of  $\sim 10\text{--}15\%$ , but once 3–4 bins are considered for the analysis, the relative gain or loss between the binning choices is at a minimal level of a few percent. Throughout this work, we will define the percentage change in the 2 $\sigma$  contour area between any pair(s) of binning setups as the relative ‘information gain or loss’ associated with the binning choices. Following the definition of the dark energy figure of merit (FOM; [Albrecht et al. 2006](#)), whereby the FOM is taken as the inverse of the area of the 2 $\sigma$   $(w_0, w_a)$  contour, our measured comparison between the areas for different binning choices similarly represents the level of improvement or degradation in the dark energy FOM value.

We note that for the equal redshift width and the equal comoving distance binning choices, the maximum number of bins that is used for the analysis is lower (4–5) than the maximum number we use for the equipopulated case. This is due to the fact that as a greater number of bins is used, there are fewer galaxies that trace the sky in a given bin, which leads to an undersampling of the observed field whereby pixels in the HEALPix map are left unfilled. For the case of a single realisation, this feature could be interpreted as a part of the mask itself and convolved with the mixing matrix formalism (see Sect. 3.3). However, for the purposes of this work in which we consider multiple hundreds of realisations, we highlight a crucial complication in that the numbers and locations of the unfilled pixels change per realisation, and then per tomographic bin, and per binning choice within each realisation.

Hence, a new coupling matrix would need to be generated for each permutation and combination of these variations since the cosmological signal is different in each case. The simulation

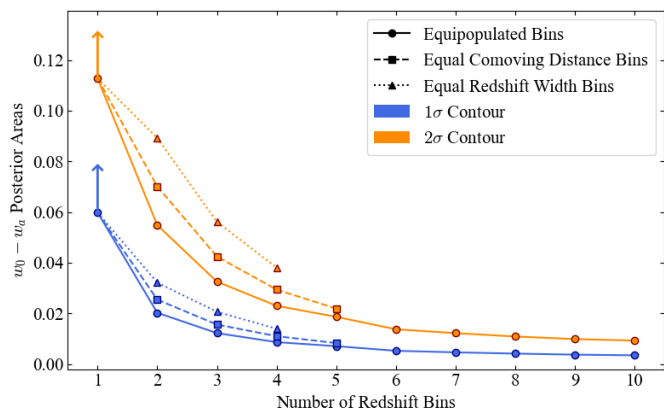


**Fig. 4.** The 1 and 2  $\sigma$  contour areas of the constraints on  $(w_0, w_a)$ , measured from the tomographic angular clustering component of our no-noise simulation. We plot the contour areas measured as a function of the number of redshift bins used in a tomographic analysis, considering the equipopulated, equal comoving distance, equally spaced in redshift binning strategies. The 1 bin measurement does not sufficiently constrain either parameter within the prior volume, hence we include a vertical arrow to denote that this data point is a lower bound.

would be both computationally impractical, and would require a fundamentally different scientific analysis that would deserve a separate, independent investigation beyond this work. Regardless, a key point we emphasise is that as the number of redshift bins used for the tomographic analysis increases, the more similar the different binning choices become, until the limit of an infinite number of bins at which point the binning choices are identical.

From Fig. 3 we find that the area of the  $(w_0, w_a)$  contours for the equipopulated binning choice starts to converge to a consistent value by  $\sim 8$  bins, beyond which there is comparatively little statistical gain in the errors on  $(w_0, w_a)$  that can be extracted by increasing the number of bins. With respect to the 2 equipopulated bin analysis, the smallest number of bins required for a closed 2  $\sigma$  contour, the use of 10 bins gains only  $\lesssim 1\%$  more information on  $(w_0, w_a)$  than the 8 bin analysis.

Since we also note that the three different binning choices converge quickly together as the number of bins are increased, we conclude that the ‘no-noise’ tomographic cosmic shear analysis is relatively insensitive to the binning choice once  $> 3$  bins are used, or to the number of bins once  $\geq 8$  bins are used, however the equal redshift width bins are marginally the best choice.

### 6.1.2. 1 $\times$ 2pt angular clustering only analysis, no-noise simulation

We present in this section the equivalent analysis of Sect. 6.1.1 for the clustering component of the 3 $\times$ 2pt signal, showing in Fig. 4 the areas of  $(w_0, w_a)$  contours derived for the three different binning choices as a function of the number of bins used for a tomographic Pseudo- $C_\ell$  power spectrum analysis.

Consistent with the cosmic shear measurements in Sect. 6.1.1, we find that for a clustering-only analysis in the absence of noise, the use of 2 bins is required to sufficiently place firm constraints on the  $(w_0, w_a)$  parameters. Comparatively, our measurements demonstrate clearly that the equipopulated tomographic bins provide the optimum constraints on  $(w_0, w_a)$ , which is in direct contrast with the results in Fig. 3 that suggest that the equipopulated binning is the worst

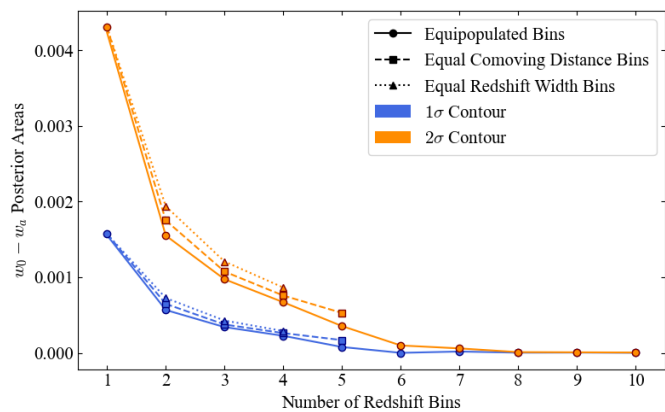


**Fig. 5.** The areas enclosed by the 1 and 2  $\sigma$  contours of the posterior constraints on  $(w_0, w_a)$ , derived from measurements of the full tomographic 3 $\times$ 2pt signal from our ‘no-noise’ mock catalogues. We plot the contour areas as a function of the number of redshift bins used in the tomographic analysis for the three different binning choices considered in this work.

choice for the shear-only measurement. Moreover, while there is a difference of only a few percent in the parameter constraints found between the three binning choices for the shear analysis, there is a much more significant effect in the clustering signal. Explicitly, we find that the degradation on the constraints on  $(w_0, w_a)$  is  $\sim 10\%$  for the equal comoving distance bins, and  $\sim 30\text{--}40\%$  for the equal redshift width bins, with respect to the equipopulated choice.

Regarding the number of tomographic bins considered, it is clear that the rate of decrease of the area enclosed by  $(w_0, w_a)$  contours converges to a constant value by 6 bins, indicating that the information gain starts to saturate beyond this point. For the equipopulated binning choice we calculate that by using 6 bins the 2  $\sigma$   $(w_0, w_a)$  contour decreases by  $\sim 80\%$  compared to a 2-bin analysis, and for every extra tomographic bin introduced beyond 7 bins, there will only be a  $\sim 1\%$  further improvement in the parameter constraints with respect to the 2-bin case.

### 6.1.3. Full 3 $\times$ 2pt analysis, no-noise simulation

For the no-noise simulations, we lastly consider a full 3 $\times$ 2pt analysis and plot the results of measurements on  $(w_0, w_a)$  in Fig. 5, demonstrating a comparison in the posterior constraints between the different binning choices.

In contrast with measurements of the cosmic shear or angular clustering components alone, we find the full 3 $\times$ 2pt data vector has sufficient constraining power to yield closed contours in  $(w_0, w_a)$  for a single redshift bin. This effectively demonstrates the joint power that the weak lensing and galaxy clustering signals have in investigating the effect of dark energy on the growth of structure in the Universe, since they probe different redshift-dependent information of the matter field along a line of sight (see also Tutusaus et al. 2020).

By increasing the number of tomographic bins, we find that the equipopulated binning choice provides the smallest errors, followed by the equal comoving distance bins and the equal redshift width bins – the same order of preference as for the clustering only analysis, which suggests that the tomographic behaviour of the clustering signal is the dominant component of the 3 $\times$ 2pt data vector. The degradation in the  $(w_0, w_a)$  constraints with respect to the equipopulated choice for a given number of

bins is ~10% for the equal comoving distance and ~20% for the equal redshift width choices, which is smaller in magnitude than for the clustering analysis. However, this is consistent with the relative performances of the different binning choices in the shear-only analysis at small numbers of bins, which highlights the conclusion that the ‘optimum’ binning choice is likely to be dependent on which observable is being targeted in the 3×2pt measurement.

We find that the contour areas, for the 3×2pt case, converge by ~6–7 bins, and we calculate that the use of 10 equipopulated bins only yields 4% more information on the  $(w_0, w_a)$  parameters than a 6 equipopulated bin analysis. This result is in strong agreement with measurements of the shear- and clustering-only constraints (Figs. 3, 4) and indicates that beyond this number of tomographic bins there is an insignificant gain in the constraints on dark energy for any and all fields of the 3×2pt signal.

The results for the noise-free ‘limiting-case’ simulations are summarised in Table 1, alongside the equivalent conclusions for a realistic noisy setup, which we discuss in detail next.

## 6.2. Realistic setup including photo- $z$ and shape noise

We now present constraints on the  $(w_0, w_a)$  parameters derived from tomographic measurements of 400 realisations of our catalogue simulation pipeline, in the presence of survey noise arising from Gaussian uncertainty in the photo- $z$  redshift estimation of galaxies, and Gaussian shape noise. The characteristics of the noise are chosen to represent the level of uncertainty that is expected to be achieved in the *Euclid* DR1 survey (see further details in Sect. 4.6). As presented in the no-noise analysis in Sect. 6.1 we examine each of the cosmic shear, angular clustering and full 3×2pt signals, and measure the 1 and 2  $\sigma$  constraints across different binning choices as a function of the number of tomographic bins used for the analysis.

### 6.2.1. 1×2pt cosmic shear only analysis, noisy simulation

In Fig. 6 we plot the 2D posterior constraints on the time evolving dark energy parameters  $(w_0, w_a)$  from noisy tomographic cosmic shear measurements using 1, 2, 3, 5, and 10 equipopulated bins.

We find that in the presence of realistic noise, the cosmic shear is relatively weakly constraining and the constraints on either parameter do not change significantly when increasing the number of tomographic bins up to 10. Additionally, we note that within the prior boundaries of the grid-based likelihood approach, only the 1  $\sigma$  contour yields an enclosed area, and the 2  $\sigma$  contour coverage in the parameter space is extended such that it is computationally intractable to constrain. However, since we sample and fully characterise the parameter volume for the 1  $\sigma$  contour for all binning numbers considered, we do not believe that the true behaviour of the 2  $\sigma$  contours will yield different results or conclusions.

We measure the area of the 1  $\sigma$  contours in the  $(w_0, w_a)$  plane in Fig. 7 for each binning choice, and find that tomographic bins equally spaced in fiducial comoving distance produce the best constraints, followed by the equal redshift width bins and finally the equipopulated bins. This represents a different order of preference compared to the no-noise set of cosmic shear measurements (Fig. 3), for which equal redshift bins give the optimum constraints. However, the relative difference between the binning choices is at a minimal level of < 5% and indicates that the gain that can be leveraged by choosing a specific binning choice for

the cosmic shear is relatively small, regardless of the presence of realistic noise.

Consistent with the 2D contour plot, we also find only a small reduction in the  $(w_0, w_a)$  area going from 1 to 10 equipopulated bins of ~20%, which is a considerably lower gain than in the no-noise simulation, which demonstrates a > 95% gain between the same number of equipopulated bins. Additionally, we find that the use of 10 equipopulated bins leads to only a 3% decrease in the area of the  $(w_0, w_a)$  contour compared to a 7-bin analysis, which is strongly consistent with the results of the no-noise simulation in Sect. 6.1. This suggests that the saturation point at which we can optimise measurements on dark energy is reached at the use of ~7 bins for a tomographic analysis of the cosmic shear signal.

We conclude that, for the cosmic shear signal, the improvement on the dark energy constraints afforded by the tomographic approach is limited by the uncertainties present in a realistic experiment, and arbitrarily increasing the number of redshift bins used for analysis may not significantly or clearly improve the results.

The simulated uncertainties from the shape noise in an individual galaxy’s shear estimate, and the photo- $z$  uncertainties, which result in overlap in the redshift distributions of different tomographic bins, will both lead to a decrease in the constraining power. It is not necessarily straightforward to determine which one contributes more to the overall degradation here. One could explore simulations in which there is shape noise included but no photo- $z$  uncertainty, and vice versa, and conduct a similar analysis to investigate how the  $(w_0, w_a)$  constraints behave in each scenario. In particular, the former case would be more analogous to a spectroscopic weak lensing survey, in which the redshifts are precisely known and tomographic bins do not overlap. However, the fundamental survey characteristics such as the redshift range, survey footprint, and number density on the sky would change, and fundamentally require different tuning in our simulation parameters. It would then be difficult to make a direct comparison with the results presented here.

Additionally the reverse scenario, in which photo- $z$  uncertainties are included but shape noise is not present in the simulation, is unachievable in a real observation since observed galaxies have an intrinsic shape. As such, we consider that both of these intermediate simulation setups are beyond the scope of this work, but would nonetheless be interesting to explore in a future study.

### 6.2.2. 1×2pt angular clustering only analysis, noisy simulation

In this section we explore the tomographic constraints made on  $(w_0, w_a)$  by the clustering component of the 3×2pt signal in the noisy simulation. In Fig. 8 we show the 2D contours measured from varying the number of redshift bins used in the equipopulated binning choice, and in Fig. 9 we plot the areas enclosed by the 1 and 2  $\sigma$  contours in the  $(w_0, w_a)$  plane as a function of the number of tomographic bins, for all three binning choices considered.

By inspecting Fig. 8, we find in particular that the shapes of the contours in the  $(w_0, w_a)$  plane for the clustering analysis are drastically different than the equivalent contour shapes derived from the cosmic shear analysis in Fig. 6. This property clearly highlights the power of the 3×2pt combined probe to break degeneracies in the dark energy parameters and provide highly precise measurements of the equation of state.

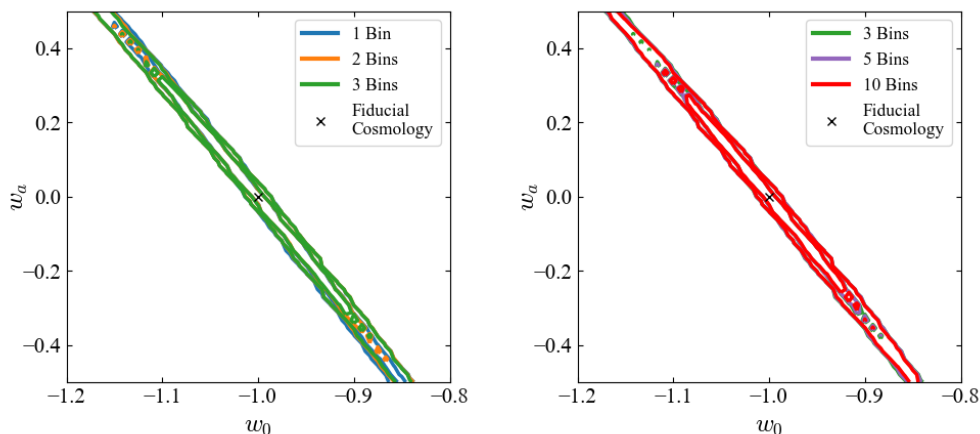


**Fig. 6.** The 1 and 2  $\sigma$  constraints on the  $(w_0, w_a)$  parameters derived from measurements of the tomographic cosmic shear signal in our noisy simulation that includes contributions from Gaussian-distributed photo- $z$  errors and Gaussian-distributed shape noise. We present the constraints for different numbers of equipopulated bins but find that the signal has relatively weak constraining power that does not significantly improve as the number of bins increases. Hence, the contours corresponding to each different number of bins lie on top of each other.

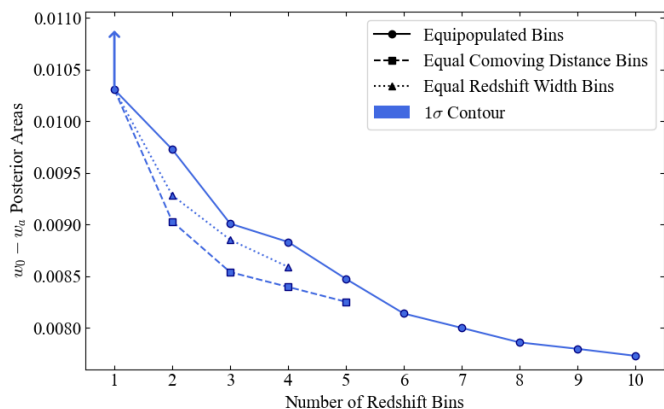


**Fig. 7.** The 1  $\sigma$  contour areas of constraints in  $(w_0, w_a)$  by measurements of the tomographic cosmic shear signal in our noisy simulation. We explore three different binning strategies and find that the 1 bin measurement does not have sufficient constraining power to generate closed contours within the prior ranges of the parameter grid. Hence, we plot the unbounded area measured within the prior ranges, and indicate that this is a lower bound of the true value by using a vertical arrow.

Collectively, the behaviour of  $(w_0, w_a)$  posterior areas measured as a function of the number of tomographic redshift bins is remarkably consistent with the no-noise simulation. In particular, the relative order of preference of the binning choices is identical across the noisy and no-noise analyses, whereby the equipopulated bins provide the optimum constraints, followed by the equal comoving distance bins and finally the equal redshift bins.

Moreover, we find that simply using 2 bins is sufficient, for all binning choices in the noisy simulations, to make measurements of  $(w_0, w_a)$  which indicates that the presence of the photo- $z$  uncertainty and shape noise does not significantly degrade the constraining power of the cosmological signal. In an absolute sense, we find that compared to the no-noise measurements, the contour areas increase by  $\sim 10\text{--}15\%$  for the equipopulated case, and  $\sim 5\%$  for both the equal comoving distance and equal redshift binning choices. We note that for the equipopulated choice,

the  $\sim 10\text{--}15\%$  increase is only due to the degradation of the cosmological signal by the photo- $z$  uncertainties, as the shape noise does not affect the angular galaxy positions and the Poisson noise is the same in both the no-noise and noisy simulations.

Most importantly, we highlight that, with and without the realistic noise included in the simulation, the improvement in the  $(w_0, w_a)$  constraints starts to saturate at 6–7 tomographic bins, which is demonstrated by the convergence and flattening of the distributions corresponding to the 1 and 2  $\sigma$  measurements in Fig. 9.

Consequently, we conclude that for an analysis of the angular clustering only, the optimum tomographic binning recommended by these results is the equipopulated choice, with  $\sim 6\text{--}7$  bins likely to be sufficient to achieve the optimum performance in the noisy case.

### 6.2.3. Full $3\times 2$ pt analysis, noisy simulation

We finally consider the effects of the tomographic binning choices on the  $(w_0, w_a)$  parameters for a full  $3\times 2$ pt analysis in the presence of noise, the target experimental and analytical setup with which to compare to the aims of the *Euclid* DR1 survey. In Fig. 10 we first plot the 1 and 2  $\sigma$   $(w_0, w_a)$  contours for tomographic measurements of the  $3\times 2$ pt signal using 1, 2, 3, 5 and 10 equipopulated bins, and in Fig. 11 we compare the areas enclosed by such contours across different binning strategies.

While a single tomographic bin used for analysis is only weakly constraining for measurements of the noisy cosmic shear and clustering signals only (Figs. 6, 8), we find that by considering the joint information contained in the  $3\times 2$ pt signal, the single bin can fully constrain the  $(w_0, w_a)$  parameters and identify a time evolving nature of the dark energy equation of state. Consequently, this result suggests that the single-bin analysis could be used as an important first-order measurement to investigate whether the photo- $z$  uncertainties and shape noise are correctly accounted for in the modelling.

With respect to the different binning choices in Fig. 11, the noisy  $3\times 2$ pt analysis is similarly consistent with the no-noise results and demonstrates that the equipopulated bins yield measurements on  $(w_0, w_a)$  that have the least error, followed by

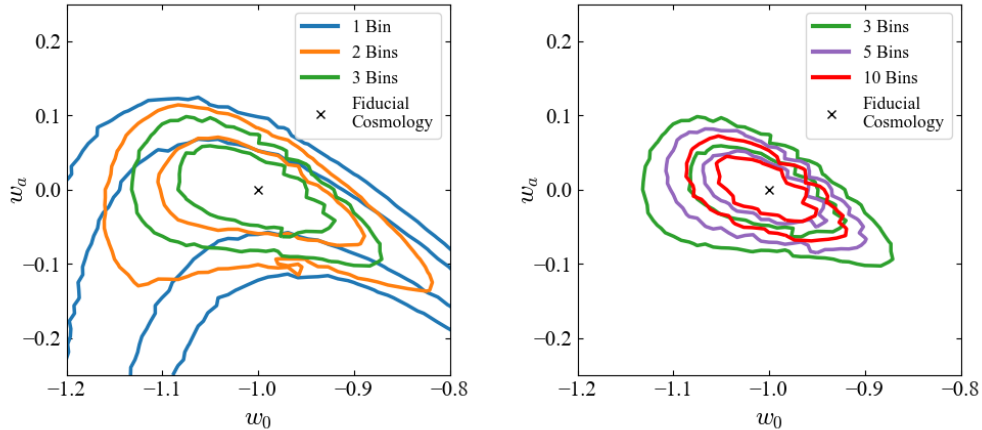


**Fig. 8.** The 1 and 2  $\sigma$  posterior constraints on  $(w_0, w_a)$  measured from the tomographic angular clustering signal in our mock catalogues which include simulated noise from Gaussian photo- $z$  uncertainties and shape noise. We show the contours for different numbers of equipopulated bins used for the tomographic analysis.

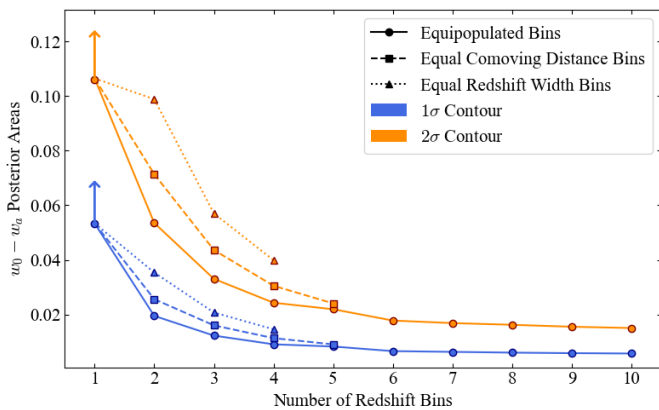


**Fig. 9.** The contour areas of the 1 and 2  $\sigma$  constraints on  $(w_0, w_a)$  for measurements of the tomographic angular clustering signal in our noisy simulation. We show the contour areas measured as a function of the number of redshift bins used, for the three different tomographic binning choices considered in this work.

the equal comoving distance bins and then the equal redshift width bins. Since the same order of preference is found in the clustering-only investigation in Sect. 6.2.2, and we find that the different binning choices only make percent level changes to the  $(w_0, w_a)$  contour areas for the shear only analysis in Sect. 6.2.1, we conclude that the performance of the different binning choices in the full 3×2pt signal is likely to be dominated by the response of the angular clustering component to the tomographic binning.

For the noisy measurements, the increase in the  $(w_0, w_a)$  areas between each binning choice in successive order of preference is more consistent with  $\sim 15\%$  at low numbers of bins (2–4), compared to  $\sim 10\%$  for the no-noise analysis, which demonstrates that in this range the specific binning choice becomes more important in deriving optimum constraints on dark energy with increasing realism in the simulation.

However, by the use of 5 tomographic bins, we find that the measured contour areas of the constraints from the equal comoving distance binning start to converge towards the equipopulated choice. Furthermore, beyond  $\sim 7$  redshift bins used, the  $(w_0, w_a)$

areas corresponding to the equipopulated constraints start to plateau, demonstrating the same saturation in the information gain present in the noisy angular clustering measurements in Fig. 11. In Table 1, we summarise our findings on the behaviour of the  $(w_0, w_a)$  contours for the different tomographic measurements of the noisy cosmic shear-only, angular clustering-only, and full 3×2pt signals. Also reported in Table 1 are the limiting case no-noise results, for all 3×2pt probes.

Empirically we find that the areas of the 1 and 2  $\sigma$  contours in the  $(w_0, w_a)$  plane, measured as a function of the number of equipopulated tomographic redshift bins used, are well described by a  $1/x$  function of the form  $y = a/x + b$  where we use the SciPy (Virtanen et al. 2020) `curve_fit` routine to derive  $(a, b) = (0.0016, 0.00037), (0.0041, 0.0011)$  for each of the 1 and 2  $\sigma$  distributions respectively.

We present these functions fit to the areas of the equipopulated constraints in Fig. 12, which demonstrates empirically how the rate of improvement in the  $(w_0, w_a)$  areas starts to decrease as the number of bins used in the tomographic analysis increases. Using the fitting functions as a baseline, we find that compared to a 1-bin analysis, the areas of the  $(w_0, w_a)$  contours decrease by 68% when using 7 bins, and 71% percent when using 10 bins, which indicates only a further 3% percent gain in information between the use of 7 and 10 bins.

By extending the fitting functions to explore the theoretical behaviour of tomographic analyses that use more than 10 bins, which we find we cannot practically measure with our method due to the presence and randomness of untraced pixels on the sky, we can estimate the area of the  $(w_0, w_a)$  contours for the particular case of 13 equipopulated bins. We note this use of 13 bins was found in *Euclid* Collaboration: Pocino et al. (2021) to improve the dark energy FOM by 15% for a 2×2pt analysis of galaxy clustering and galaxy-galaxy lensing, based on photo- $z$  studies using the *Euclid* Collaboration Flagship Simulation (*Euclid* Collaboration: Castander et al. 2024).

Using our extended fitting functions in Fig. 12, we find that the  $(w_0, w_a)$  contour areas for 13 bins decrease by 15% and 5% compared to analyses using 7 and 10 tomographic bins respectively. Additionally, by measuring the total improvement on the  $(w_0, w_a)$  constraints with respect to the single-bin analysis, we find that this corresponds to only a further 5% gain in the preci-

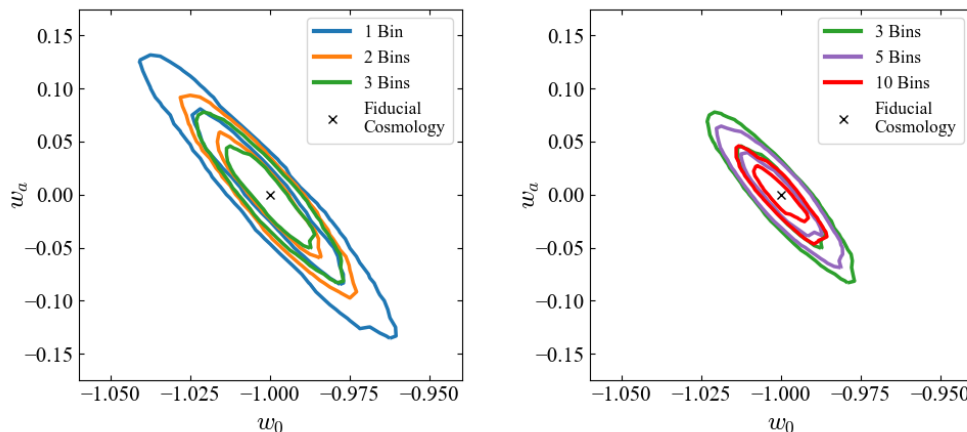


**Fig. 10.** The 1 and  $2\sigma$  constraints on  $(w_0, w_a)$  from tomographic Pseudo- $C_\ell$  measurements of the full  $3\times 2$ pt signal in our noisy simulation. We show constraints measured for different numbers of equipopulated bins used for the tomographic analysis. The cross marks the fiducial cosmology  $(w_0, w_a) = (-1, 0)$  used for the simulation.

**Table 1.** A Table summarising the behaviour of the cosmic shear component, angular clustering component, and full  $3\times 2$ pt signal for different tomographic binning choices. The summary conclusions have been evaluated from the constraints on  $(w_0, w_a)$  measured across multiple binning choices and redshift bins in tomographic analyses of our simulated catalogues for both a no-noise and noisy set up (Sects. 6.1, 6.2).

Signal	Simulation Type	Optimum Binning Choice	Optimum No. Bins	Properties
Full $3\times 2$ pt	Realistic Noise	Equipopulated	Convergence by $\sim 7$	Relative improvement between binning choices is 15% – clear motivation to use the equipopulated bins
	No-Noise	Equipopulated	Convergence by $\sim 6-7$	Relative gain between binning choices is less significant ( $\sim 10\%$ ) compared to the noisy simulation
Cosmic Shear	Realistic Noise	Equal Comoving Distance	Convergence by $\sim 7$	Minimal difference between different binning choices (percent level)
	No-Noise	Equal Redshift Width	Convergence by $\sim 8$	Only small gain by increasing the number of bins from 1 to 10 (20%, compared to $> 95\%$ for the no-noise case)
Angular Clustering	Realistic Noise	Equipopulated	Convergence by $\sim 6-7$	Minimal difference in behaviour between no-noise and noisy simulations
	No-Noise	Equipopulated	Convergence by $\sim 6-7$	Minimal difference in behaviour between no-noise and noisy simulations

sion on the parameters when increasing from 7 to 13 bins in the measurement, and a  $< 2\%$  level gain when going from 10 to 13 bins.

Overall, these results indicate that increasing the number of tomographic bins beyond 10 leads to improvements in the  $(w_0, w_a)$  constraints that are less substantial than those found by [Euclid Collaboration: Pocino et al. \(2021\)](#). However, we note that each of these results has been determined using different methods and with different assumed survey characteristics.

In particular, the latter study considers a  $2\times 2$ pt analysis and focuses on the configuration and cosmological information that is expected to be obtained from the complete *Euclid* survey, rather than just the first data release (DR1) that our analysis has

focused on. Consequently, the underlying  $n(z)$ , spatial density of galaxies on the sky, and scale cuts taken for the  $3\times 2$ pt signal considered in [Euclid Collaboration: Pocino et al. \(2021\)](#) will be different than those considered in this study. Additionally, while we have considered an analytical method to simulate galaxy redshifts and their uncertainties, [Euclid Collaboration: Pocino et al. \(2021\)](#) adopted machine learning methods to estimate the photometric redshifts.

We note for our analysis that there are still errors associated with the data points due to the fact we can only work with a finite number of realisations, which in an ideal case would be included in the derivation of the fitting function and its parameters. As such, the relative statistical gains and comparisons we



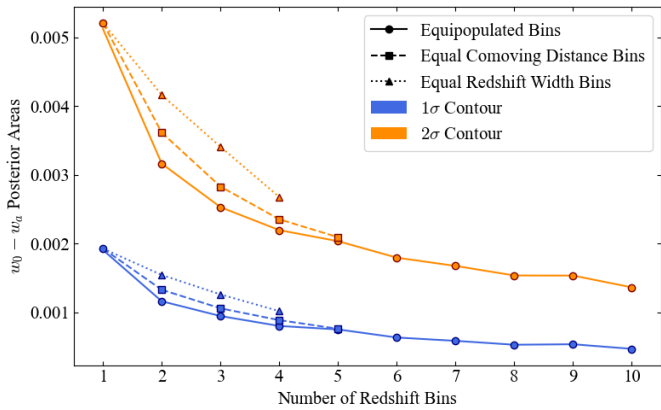


**Fig. 11.** The contour areas enclosed by the 1 and 2  $\sigma$  constraints on the dark energy ( $w_0, w_a$ ) parameters, measured for the full 3×2pt signal in the presence of Gaussian shape noise and photo- $z$  uncertainty. We vary the number of redshift bins used for each of the equipopulated, equally spaced in fiducial comoving distance, and equal redshift width binning strategies.

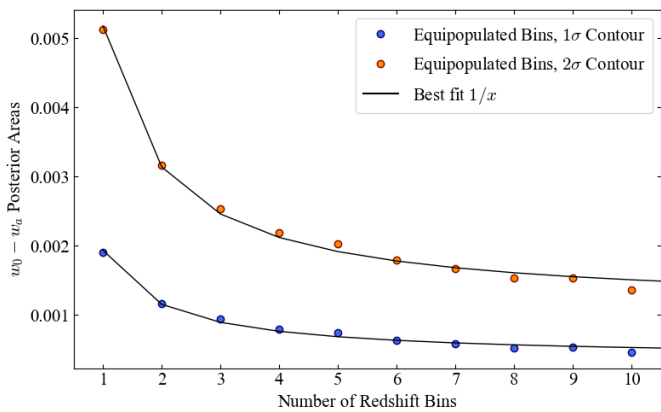


**Fig. 12.** The areas of the 1 and 2  $\sigma$  constraints on  $(w_0, w_a)$ , measured from our noisy catalogue simulations, plotted in circular markers as a function of the number of equipopulated bins used for the tomographic analysis. In black solid lines, we plot the best fit functions of the form  $y = a/x + b$  that we fit to these data sets, evaluated using the SciPy `curve_fit` routine.

present here should be considered only as a guide and not absolute results. In principle, a quantification of the errors could be achieved for example by repeating the entire analysis to measure the set of  $(w_0, w_a)$  contour areas over multiple batches of 400 realisations, and then examining the deviation across all batches. However, this is unfortunately computationally expensive and impractical to achieve in this study.

Nonetheless, we assert that the errors will be equivalent in magnitude for the different binning choices considered, and hence conclude that for a full 3×2pt tomographic analysis of our simulated *Euclid* DR1-like catalogues, in the presence of realistic noise, the optimum binning choice is the equipopulated case.

While there perhaps could still be merit in using 10 tomographic bins to extract a few more percent precision in  $(w_0, w_a)$ , we note that the use of more bins would increase the computational expense. Moreover, it is likely that any potential benefits are only realisable, within the framework of a theoretical study, such as the one presented here, where one has full control and knowledge of the uncertainties that are introduced.

Comparatively, for a real Stage IV analysis it is likely that this extra information probed by increasing the number of bins beyond  $\sim 7$  will be difficult to leverage, especially in light of the additional model and inference complexity that is due to effects we do not consider here, such as the shear bias in the shape measurements of galaxies (e.g. Hirata & Seljak 2003, Jansen et al. 2024, Euclid Collaboration: Congedo et al. 2024), the effects of magnification in the galaxy sample and further high order terms (e.g. Duncan et al. 2022, Deshpande et al. 2020, Euclid Collaboration: Deshpande et al. 2024), or the effects of marginalisation over other cosmological parameters within their prior ranges.

We note additionally the impact of intrinsic alignments on 3×2pt cosmology (e.g. Troxel & Ishak 2015), which we do not model in this study. It has been proposed that the systematic effects of intrinsic alignments can be quantified by the use of tomography (King & Schneider 2002), and we highlight that such an investigation could be a possible extension of this work for the future.

Lastly, we note that the true errors in the photo- $z$  estimates, the shear estimates and/or the measured power spectra may not be purely Gaussian (e.g. Takada & Jain 2009). We explore an example of this scenario in the following section (Sect. 7) where we consider the effects of catastrophic photo- $z$  uncertainties in the estimation of the galaxy redshifts and the subsequent impact on the inference on the dark energy parameters.

## 7. Catastrophic photo- $z$ uncertainties

In this section we demonstrate the flexibility of our simulation method to incorporate further astrophysical or survey-like effects by injecting catastrophic photo- $z$  uncertainties into our catalogue simulation, and then propagating the resulting biased measurements into cosmological constraints on  $(w_0, w_a)$ .

Photo- $z$  estimation codes can mis-identify features in the spectral energy distribution (SED) of a galaxy, leading to a measured redshift that significantly fails to recover the true redshift of the galaxy. For the purposes of the 3×2pt signal, the mis-estimated galaxy redshift will lead to an incorrect interpretation of the structure along the line of sight that has induced the shear in the galaxy, which will limit our ability to make accurate measurements of dark energy and its possible time-evolving behaviour.

In order to achieve its science goals, *Euclid* will target a 5% level of contamination by catastrophic photo- $z$  errors (Lau-reijs et al. 2011) in the real analysis. Hence, we introduce the effects of this systematic into our simulation by randomly selecting 5% of our galaxy sample in the noisy setup and distorting their estimated redshift measurement in the catalogue to a catastrophic estimation using Eq. (43). The relation between the true redshift and the catastrophic redshift ( $z_{\text{cata}}$ ) modelled here is governed by the ratio between the rest-frame wavelength of a break feature in the SED and the wavelength that is predicted by the photo- $z$  estimation technique. As a first-order investigation, we consider catastrophic errors that result from the rest-frame Lyman- $\alpha$  line being confused with the Balmer and D4000 breaks, i.e. taking the pairs  $[\lambda_{\text{break-rf}}, \lambda_{\text{break-cata}}] = [\text{Ly-}\alpha, \text{Balmer-break}], [\text{Ly-}\alpha, \text{D4000-break}]$  and splitting the 5% contamination equally between the two pairs of misidentified features. We finally model the resulting catastrophic photo- $z$  estimate as a Gaussian-distributed value with mean  $z_{\text{cata}}$  and standard deviation  $\sigma_{z_{\text{cata}}} = 0.1$ .

Following this procedure, we measure the tomographic Pseudo- $C_\ell$  power spectra from these biased mock catalogues using the standard technique adopted in this work as described in

Sect. 3.2. The presence of the catastrophic photo- $z$  errors will induce a change  $\Delta C_\ell$  in the measured power spectra compared to the standard noisy case. In order to determine the impact of this bias on the dark energy ( $w_0, w_a$ ) constraints, we 1) add the measured  $\Delta C_\ell$  onto the true, theoretical  $3\times 2$ pt data vector of the fiducial cosmology, and 2) perform the grid-based Gaussian likelihood analysis on this distorted  $3\times 2$ pt signal using an underlying tomographic redshift distribution  $n(z)$  and a numerical covariance matrix that have both been derived from the simulations that include Gaussian noise. As such, the final constraints on ( $w_0, w_a$ ) that we measure will be directly comparable to the Gaussian noise-like results of Sect. 6.2.3. Any difference will be due to the 5% contamination by catastrophic photo- $z$ s, where we do not retain knowledge of which individual galaxies are affected, and the use of a covariance matrix that does not include sufficient information on the catastrophic photo- $z$ s. As such, we emphasise that we do not attempt to mitigate against the presence of the catastrophic outliers in order to derive our dark energy constraints, which we expect to be pessimistic. Comparatively, a real analysis could attempt to correct for these uncertainties in the assumed  $n(z)$  distribution, or as a nuisance parameter to marginalise over in the inference.

In Fig. 13 we show the 1, 2 and 3  $\sigma$  constraints on ( $w_0, w_a$ ) for three different tomographic analyses of the full  $3\times 2$ pt signal: a single redshift bin; 5 equipopulated bins and 10 equipopulated bins, comparing in blue the results from the Gaussian noise-like simulations in Sect. 6.2.3 and in red the results from the catastrophic photo- $z$  analysis.

We find that the measurements across the three different tomographic binning choices all consistently yield the constraints ( $w_0 > -1, w_a < 0$ ). These parameters are strongly biased from the underlying  $\Lambda$ CDM cosmology and demonstrate that the presence of a 5% level of contamination from catastrophic photo- $z$ s, if entirely unaccounted for in the modelling, would lead us to infer significantly incorrect conclusions on a time-evolving behaviour of the dark energy equation of state. Indeed, such effects of catastrophic photo- $z$  uncertainties for weak lensing surveys have been extensively studied in the literature, e.g. Hearin et al. (2010), Ma et al. (2006), and Sun et al. (2009), for which our results act to support and consolidate.

Since the constraining power of the  $3\times 2$ pt signal increases with the number of redshift bins used for the tomographic analysis, the statistical disagreement with the true underlying cosmology also increases with the number of tomographic bins. Explicitly, for a single-bin analysis we find that if the catastrophic outliers are not modelled in the  $3\times 2$ pt data vector, the power spectrum measurements are in tension with  $\Lambda$ CDM at  $\sim 3\sigma$ , while for 5 and 10 bins the tension is at a  $> 5\sigma$  level. It is clear that the dark energy ( $w_0, w_a$ ) parameters are highly sensitive to the catastrophic photo- $z$  uncertainties. Since we do not attempt to correct for these errors to derive the constraints presented here, these results aim to quantify the extent to which these uncertainties would need to be minimised or mitigated in the real analysis in order to determine the true nature of dark energy.

In addition to the biased recovery of the true cosmology, we find that the presence of the catastrophic photo- $z$  errors leads to unusual structures in the 2D posterior. For our standard noise and noisy simulations (for which the photo- $z$  uncertainties are purely Gaussian), we expect that the  $3\times 2$ pt measurements will generate smooth, elliptical contours, as demonstrated in Fig. 10. In contrast, for the 5- and 10-bin analyses we see that the contours are less elliptical in shape and have multiple, non-contiguous regions in the catastrophic photo- $z$  analysis. We do not attribute these features to an imprecision in the sampling

of the parameter space, as we have experimented increasing the resolution of the 2D grid and found the same results. Rather, we believe that these features are due to the  $\Delta C_\ell$  change in the  $3\times 2$ pt power spectra that the catastrophic redshift errors induce. The  $C_\ell$  bias is non-trivial and random across all redshifts, and hence the space of cosmological models in ( $w_0, w_a$ ) that the resulting power spectra are compatible with is complex and discontinuous.

We conclude that the introduction of the 5% contamination by catastrophic photo- $z$  uncertainties can severely compromise the attempt to measure accurate cosmological constraints from the  $3\times 2$ pt signal if not adequately mitigated. In particular, the constraints yield a best fit model that is in tension with  $\Lambda$ CDM at  $> 5\sigma$  for analyses using 5 or more tomographic redshift bins, and the posterior distributions in ( $w_0, w_a$ ) demonstrate sharp, discontinuous features.

Additionally, we note that catastrophic photo- $z$  uncertainties may be caused by further effects in addition to the confusion between the Lyman- $\alpha$  line, and the Balmer and D4000 breaks that we have considered throughout this work. For example, ‘uniform’ catastrophic outliers may be caused when the light from a galaxy is contaminated by light from a nearby source on the sky which is at a different redshift (see e.g. Hearin et al. 2010). A full investigation into the nature of the bias induced by further causes of catastrophic photo- $z$  errors is beyond the scope of this work. However, we emphasise that our simulation framework has the flexibility to incorporate a range of different distributions for the catastrophic photo- $z$  uncertainty that could be examined in a future study.

These results emphasise that an accurate modelling of the catastrophic photo- $z$  errors would need to be accounted for in the theoretical model of the cosmological signal, the covariance matrix, and the likelihood distribution. Further methods to mitigate against catastrophic uncertainties include marginalisation over a nuisance parameter (Bernstein & Huterer 2010) capturing catastrophic errors; or selectively removing galaxies from the redshift distribution (Hearin et al. 2010), for example by monitoring the posterior likelihood distribution of galaxy redshift estimates (Nishizawa et al. 2010).

## 8. Discussion and conclusions

Investigations attempting to determine an ‘optimum’ binning configuration for a tomographic  $3\times 2$ pt analysis, mostly using machine learning or numerical methods (Taylor et al. 2018a, Kitching et al. 2019, Sipp et al. 2021, Euclid Collaboration: Pociño et al. 2021, Zuntz et al. 2021, see Sect. 2), have returned inconsistent conclusions on both the binning choice and number of bins that should be targeted. In this work, we present an alternative method to explore the tomographic binning with the aim to mimic a real survey and subsequent cosmological analysis in a robust and comprehensive manner. We develop a simulation pipeline that generates multiple realisations of mock galaxy catalogues for a Stage IV-like survey, which are constructed by generating a set of correlated  $3\times 2$ pt 2D maps on the sky, that sample a target redshift range, to model the full 3D cosmological information in the Universe.

From our mock catalogues we measure the  $3\times 2$ pt Pseudo- $C_\ell$  power spectra, evaluated over an approximation of the *Euclid* DR1 footprint, for a range of tomographic configurations. We propagate these measurements into a grid-based Gaussian likelihood analysis to place constraints on the dark energy equation of state parameters ( $w_0, w_a$ ), and derive the optimum binning

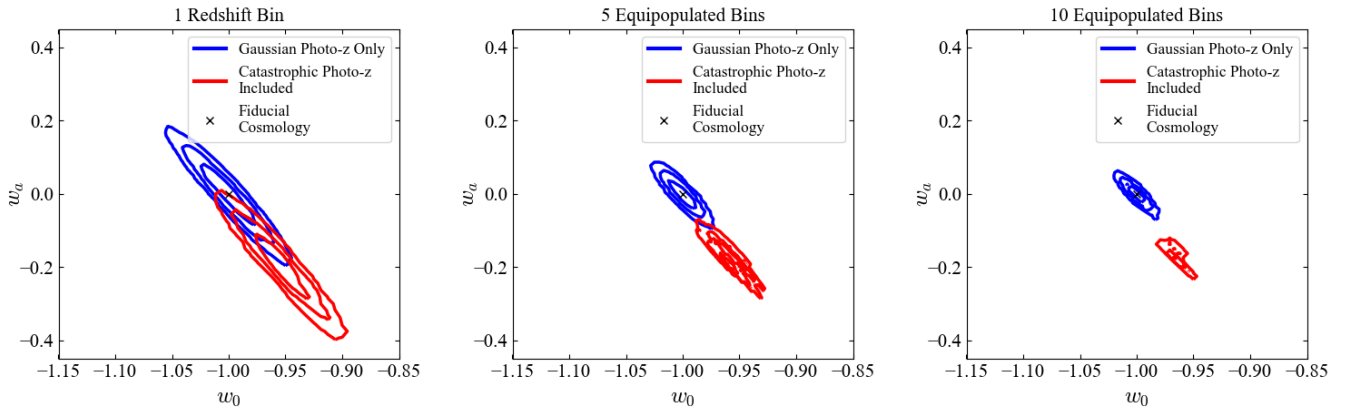


**Fig. 13.** Constraints on the dark energy ( $w_0, w_a$ ) parameters measured from: Blue) simulations that include only Gaussian shape noise and Gaussian photo- $z$  uncertainties, and Red) simulations that include Gaussian shape noise, Gaussian photo- $z$  uncertainties, and a 5% level of catastrophic photo- $z$  errors (outliers) that result from the Lyman- $\alpha$  line in the galaxy SED being misidentified as the Balmer and D4000 break features. From left to right we plot the constraints derived from tomographic analyses of the full 3×2pt signal using a single redshift bin, 5 equipopulated bins and 10 equipopulated bins.

choice by comparing the size of the contours in  $(w_0, w_a)$  across all tomographic binning configurations considered.

For a limiting case ‘no-noise’ simulation in which we do not consider any effects of redshift uncertainties due to photo- $z$  estimation techniques, or shape noise associated with the observed shear of a galaxy, we find that the optimum binning choice for a full 3×2pt analysis is redshift bins that are equally populated with galaxies. For the angular galaxy clustering signal, the optimum binning choice is also the equipopulated case, which is likely to be the dominant component of the 3×2pt data vector. However for an analysis of the cosmic shear only, bins that are equally spaced in redshift yield the best constraints on  $(w_0, w_a)$  which indicates that the optimum binning choice is dependent on which observable is targeted.

For a more realistic simulation in which we include Gaussian shape noise and Gaussian photo- $z$  uncertainties in the mock catalogues, we find that the equipopulated bins remain the best choice to measure  $(w_0, w_a)$  for the full 3×2pt and angular clustering only analyses. However, the cosmic shear signal itself gives the best constraints when bins that are equally spaced in fiducial comoving distance are used – where the fiducial cosmology we work with is the standard  $\Lambda$ CDM.

We note that for a different underlying cosmology, the redshift bin boundaries for the equal comoving distance binning choice would change. However, we emphasise that as greater numbers of tomographic bins are used for the analysis, the derived constraints on  $(w_0, w_a)$  for each binning choice would converge together regardless of the fiducial cosmology. Hence, we do not expect that our results would change significantly in this range.

Collectively, we find that the relative gain or loss between the different binning choices is least significant for the cosmic shear signal, at the level of a few percent in the  $(w_0, w_a)$  contour areas, both with and without noise included in the simulation. This result suggests that the cosmic shear signal is fundamentally less sensitive to the tomographic binning choice, and there may not be significant benefit in targeting a given binning choice in the real analysis.

In comparison, we find that the difference in size of the  $(w_0, w_a)$  contour areas, between the different binning choices in successive order of preference, is  $\sim 10\%$  for the full 3×2pt and

clustering-only measurements in the no-noise setup, and slightly more amplified at  $\sim 10\text{--}15\%$  for the realistic noise simulation. We conclude for these signals that the gain is considerable and it provides clear motivation to choose the equipopulated binning for a real Stage IV analysis.

With respect to the number of redshift bins chosen for tomography, we expect that the rate of information gain will decrease as the number of bins increases, until a point at which the area of the  $(w_0, w_a)$  contours will converge to a consistent value that does not continue to improve when arbitrarily adding more bins for the tomographic analysis. For each of the cosmic shear and clustering components individually, we find that this convergence is reached at  $\sim 6\text{--}8$  bins in the 1 and  $2\sigma$  contours across both the no-noise and noisy simulations. For each of these signals the minimum number of bins required to fully constrain the dark energy parameters is 2, and using this measurement as a baseline we find that for both components in the noisy setup there is only a further  $\mathcal{O}(1\%)$  level improvement in the  $(w_0, w_a)$  constraints when increasing the number of tomographic bins from 7 to 10.

In terms of the full 3×2pt analysis, we find a clear convergence in the  $(w_0, w_a)$  areas at the use of  $\sim 7$  tomographic redshift bins for the no-noise measurements. For the noisy simulation the behaviour is similar and empirically we find that the rate at which the  $(w_0, w_a)$  contour areas decrease, as a function of the number of equipopulated tomographic redshift bins, is well described by a  $1/x$  function of the form  $y = a/x + b$  where we derive  $(a, b) = (0.0016, 0.00037), (0.0041, 0.0011)$  for the 1 and  $2\sigma$  trends respectively. Using this function to theoretically predict the contour size for the 13 bin analysis that has been proposed for *Euclid* (e.g. [Euclid Collaboration: Pocino et al. 2021](#)), we measure the total gain in information with respect to the single redshift bin constraints, and find that there is only a 5% further improvement in measurements of  $(w_0, w_a)$  when going from 7 to 13 bins.

For higher numbers of redshift bins, the 3×2pt data vector becomes larger and the information gain on  $(w_0, w_a)$  becomes increasingly limited by the demand for accuracy in the covariance matrix. This manifests as an increase in excess random noise in the numerical covariance matrix used in this work, but the

trade-off would also be important to consider in a real analysis, particularly where an analytical covariance may be used.

Furthermore, there will be additional uncertainties present in a real survey, such as from the shear calibration, redshift-dependent astrophysical systematics (e.g. intrinsic alignments), and the nature of non-Gaussianities in the likelihood or the errors. The accuracy to which these are accounted for will then limit whether the information gain can actually be realised, and hence the extent to which arbitrarily increasing the number of redshift bins would be preferred. In principle, the flexibility of our simulation approach offers the capability to include the effects of these additional uncertainties in our mock catalogues and then propagate the resulting power spectra into cosmological constraints on  $(w_0, w_a)$ . We note that such additional effects may lead to a convergence in the  $(w_0, w_a)$  areas at an even lower number of redshift bins or yield a different order of preference for the binning choice; however such a study is beyond the scope of this paper.

Nevertheless, for the  $3 \times 2$ pt and angular clustering analyses such additional effects would have to be considerable since the relative difference between the different binning choices is reasonably significant at  $\sim 10\text{--}15\%$ . Hence we reassert that the best performing binning strategy, the equipopulated case, is likely to be a good choice for these observables in the DR1 analysis for *Euclid*. Furthermore, in the limit that the observation is dominated by shape noise and photo- $z$  uncertainty, we emphasise our conclusion that any given binning choice is unlikely to result in significant degradation in the constraints achievable using the cosmic shear signal on  $(w_0, w_a)$ .

Additionally, we note that throughout this work we have considered a fixed scale range  $100 \leq \ell \leq 1500$  for deriving dark energy constraints from tomographic Pseudo- $C_\ell$  power spectra. For the real analysis of the *Euclid* sample, we expect that the upper limit is likely to be a conservative estimate for the cosmic shear analysis and an optimistic estimate for the angular clustering. The effect of changing these angular scale cuts on conclusions of the optimum tomographic binning strategy could represent an informative extension of this study. However, such an investigation would need to carefully consider a range of further modelling and analytical choices to adopt for the  $3 \times 2$ pt measurements. In particular, as we probe increasingly smaller scales by including larger  $\ell$  modes, the assumptions of the constant galaxy bias or even the Gaussianity of the underlying  $3 \times 2$ pt fields are likely to break down.

Furthermore, there is a considerable range of freedom in how a scale cut could be applied to each component of the  $3 \times 2$ pt signal, and it is not trivial to predict the degeneracy in the behaviour of the  $(w_0, w_a)$  constraints when different combinations of the probes have different cuts applied. We further note that the practical and computational limitations of the simulation-based method will be exacerbated as smaller scales are introduced. Notably, the smaller scales will increase the presence of the unphysical pixels realised on the sky (those with  $\delta_g < 1$  which mask out observable regions of the mock survey, see also Sect. 4.3); and may increase the shot noise in the numerical covariance matrix if the  $3 \times 2$ pt power spectra need to be resolved to a greater number of angular bandpowers to capture the small scale information. Hence, we consider an investigation into the impact of the chosen angular scales on tomography as an important study, but beyond the scope of this work.

Lastly, we have considered the effects of catastrophic photo- $z$  uncertainties for our dark energy constraints, whereby the errors associated with the redshift estimation of galaxies is no longer Gaussian. We inject a 5% level of contamination by catastrophic

photo- $z$  errors, randomly distributed across all redshifts, caused by the Lyman- $\alpha$  line being confused with the Balmer and D4000 breaks.

If such a contamination is unaccounted for in the modelling, we find that a full  $3 \times 2$ pt analysis using a single tomographic bin would return measurements of  $(w_0, w_a)$  that are in tension with the fiducial  $\Lambda$ CDM cosmology at  $\sim 3\sigma$ . For a 5- or 10-bin analysis with equipopulated bins, we find that the  $(w_0, w_a)$  constraints are in extreme tension with  $\Lambda$ CDM at  $> 5\sigma$ , and there are sharp and discontinuous features in the posterior distribution. This result reaffirms the necessity to minimise the presence of these catastrophic redshift uncertainties, and to develop techniques that model their effects in the cosmological signal, the covariance and even the nature of the likelihood distribution.

*Acknowledgements.* We thank colleagues in the *Euclid* Consortium for useful comments and feedback. We also thank Duncan Austin, Tom Harvey and Erik Rosenberg (JBCA) for their helpful discussions around modelling approaches for photo- $z$  outliers and the numerical covariance matrix. JHWW acknowledges support in the form of a PhD studentship from the UK Science and Technology Facilities Council (STFC) and the University of Manchester Centre for Doctoral Training. MLB and CAJD acknowledge funding from the STFC (grant number ST/X001229/1). The *Euclid* Consortium acknowledges the European Space Agency and a number of agencies and institutes that have supported the development of *Euclid*, in particular the Agenzia Spaziale Italiana, the Austrian Forschungsförderungsgesellschaft funded through BMK, the Belgian Science Policy, the Canadian *Euclid* Consortium, the Deutsches Zentrum für Luft- und Raumfahrt, the DTU Space and the Niels Bohr Institute in Denmark, the French Centre National d'Études Spatiales, the Fundação para a Ciência e a Tecnologia, the Hungarian Academy of Sciences, the Ministerio de Ciencia, Innovación y Universidades, the National Aeronautics and Space Administration, the National Astronomical Observatory of Japan, the Nederlandse Onderzoeksschool Voor Astronomie, the Norwegian Space Agency, the Research Council of Finland, the Romanian Space Agency, the State Secretariat for Education, Research, and Innovation (SERI) at the Swiss Space Office (SSO), and the United Kingdom Space Agency. A complete and detailed list is available on the *Euclid* web site ([www.euclid-ec.org](http://www.euclid-ec.org)).

## References

- Abbott, T. M. C., Aguena, M., Alarcon, A., et al. 2022, *Phys. Rev. D*, 105, 023520
- Abbott, T. M. C., Aguena, M., Alarcon, A., et al. 2023, *Phys. Rev. D*, 107, 083504
- Ahumada, R., Allende Prieto, C., Almeida, A., et al. 2020, *ApJS*, 249, 3
- Alam, S., Ata, M., Bailey, S., et al. 2017, *MNRAS*, 470, 2617
- Albrecht, A., Bernstein, G., Cahn, R., et al. 2006, *arXiv/astro-ph*, 0609591
- Bartelmann, M. & Schneider, P. 2001, *Phys. Rep.*, 340, 291
- Benjamin, J., Van Waerbeke, L., Heymans, C., et al. 2013, *MNRAS*, 431, 1547
- Bernstein, G. & Huterer, D. 2010, *MNRAS*, 401, 1399
- Brout, D., Scolnic, D., Popovic, B., et al. 2022, *ApJ*, 938, 110
- Brown, M. L., Castro, P. G., & Taylor, A. N. 2005, *MNRAS*, 360, 1262
- Castro, P. G., Heavens, A. F., & Kitching, T. D. 2005, *Phys. Rev. D*, 72, 023516
- Crittenden, R. G., Natarajan, P., Pen, U.-L., & Theuns, T. 2002, *ApJ*, 568, 20
- Deshpande, A. C., Kitching, T. D., Cardone, V. F., et al. 2020, *A&A*, 636, A95
- DESI Collaboration, Adame, A. G., Aguilar, J., et al. 2024, *arXiv e-prints*, [arXiv:2404.03002](https://arxiv.org/abs/2404.03002)
- DESI Collaboration, Aghamousa, A., Aguilar, J., et al. 2016, *arXiv e-prints*, [arXiv:1611.00036](https://arxiv.org/abs/1611.00036)
- Dodelson, S. & Schneider, M. D. 2013, *Phys. Rev. D*, 88, 063537
- Duncan, C. A. J., Harnois-Déraps, J., Miller, L., & Langedijk, A. 2022, *MNRAS*, 515, 1130
- Euclid* Collaboration: Blanchard, A., Camera, S., Carbone, C., et al. 2020, *A&A*, 642, A191
- Euclid* Collaboration: Castander, F., Fosalba, P., Stadel, J., et al. 2024, *A&A*, submitted, [arXiv:2405.13495](https://arxiv.org/abs/2405.13495)
- Euclid* Collaboration: Congedo, G., Miller, L., Taylor, A. N., et al. 2024, *A&A*, submitted, [arXiv:2405.00669](https://arxiv.org/abs/2405.00669)
- Euclid* Collaboration: Deshpande, A. C., Kitching, T., Hall, A., et al. 2024, *A&A*, 684, A138
- Euclid* Collaboration: Desprez, G., Paltani, S., Coupon, J., et al. 2020, *A&A*, 644, A31
- Euclid* Collaboration: Ilbert, O., de la Torre, S., Martinet, N., et al. 2021, *A&A*, 647, A117

- Euclid Collaboration: Mellier, Y., Abdurro'uf, Acevedo Barroso, J., Achúcarro, A., et al. 2024, A&A, submitted, arXiv:2405.13491
- Euclid Collaboration: Paykari, P., Kitching, T., Hoekstra, H., et al. 2020, A&A, 635, A139
- Euclid Collaboration: Pocino, A., Tutusaus, I., Castander, F. J., et al. 2021, A&A, 655, A44
- Euclid Collaboration: Tessore, N., Joachimi, B., Loureiro, A., et al. 2024, arXiv e-prints, arXiv:2408.16903
- Giocoli, C., Jullo, E., Metcalf, R. B., et al. 2016, MNRAS, 461, 209
- Górski, K. M., Hivon, E., Banday, A. J., et al. 2005, ApJ, 622, 759
- Hearin, A. P., Zentner, A. R., Ma, Z., & Huterer, D. 2010, ApJ, 720, 1351
- Heavens, A. 2003, MNRAS, 343, 1327
- Hikage, C., Oguri, M., Hamana, T., et al. 2019, PASJ, 71, 43
- Hikage, C., Takada, M., Hamana, T., & Spergel, D. 2011, MNRAS, 412, 65
- Hilbert, S., Hartlap, J., White, S. D. M., & Schneider, P. 2009, A&A, 499, 31
- Hildebrandt, H., Viola, M., Heymans, C., et al. 2017, MNRAS, 465, 1454
- Hirata, C. & Seljak, U. 2003, MNRAS, 343, 459
- Hivon, E., Górski, K. M., Netterfield, C. B., et al. 2002, ApJ, 567, 2
- Hu, W. 1999, ApJ, 522, L21
- Hu, W. 2002, Phys. Rev. D, 66, 083515
- Huterer, D. 2002, Phys. Rev. D, 65, 063001
- Jain, B. & Taylor, A. 2003, Phys. Rev. Lett., 91, 141302
- Jansen, H., Tewes, M., Schrabback, T., et al. 2024, A&A, 683, A240
- Jouvel, S., Kneib, J. P., Bernstein, G., et al. 2011, A&A, 532, A25
- Kaiser, N. 1992, ApJ, 388, 272
- Kamionkowski, M., Babul, A., Cress, C. M., & Refregier, A. 1998, MNRAS, 301, 1064
- Kilbinger, M. 2015, Reports on Progress in Physics, 78, 086901
- King, L. & Schneider, P. 2002, A&A, 396, 411
- Kitching, T. D., Heavens, A. F., Alsing, J., et al. 2014, MNRAS, 442, 1326
- Kitching, T. D., Heavens, A. F., Taylor, A. N., et al. 2007, MNRAS, 376, 771
- Kitching, T. D., Taylor, P. L., Capak, P., Masters, D., & Hoekstra, H. 2019, Phys. Rev. D, 99, 063536
- Kohonen, T. 1990, Proceedings of the IEEE, 78, 1464
- Krause, E. & Hirata, C. M. 2010, A&A, 523, A28
- Laureijs, R., Amiaux, J., Arduini, S., et al. 2011, arXiv e-prints, arXiv:1110.3193
- Lewis, A., Challinor, A., & Lasenby, A. 2000, ApJ, 538, 473
- Lewis, A., Challinor, A., & Turok, N. 2001, Phys. Rev. D, 65, 023505
- Limber, D. N. 1953, ApJ, 117, 134
- Loureiro, A., Moraes, B., Abdalla, F. B., et al. 2019, MNRAS, 485, 326
- LoVerde, M. & Afshordi, N. 2008, Phys. Rev. D, 78, 123506
- LSST Science Collaboration, Abell, P. A., Allison, J., et al. 2009, arXiv e-prints, arXiv:0912.0201
- Ma, Z., Hu, W., & Huterer, D. 2006, ApJ, 636, 21
- Nicola, A., Alonso, D., Sánchez, J., et al. 2020, JCAP, 03, 044
- Nishizawa, A. J., Takada, M., Hamana, T., & Furusawa, H. 2010, ApJ, 718, 1252
- Peebles, P. J. E. 1973, ApJ, 185, 413
- Perlmutter, S., Aldering, G., Goldhaber, G., et al. 1999, ApJ, 517, 565
- Planck Collaboration: Aghanim, N., Akrami, Y., Ashdown, M., et al. 2020, A&A, 641, A6
- Riess, A. G., Filippenko, A. V., Challis, P., et al. 1998, AJ, 116, 1009
- Schmidt, B. P., Suntzeff, N. B., Phillips, M. M., et al. 1998, ApJ, 507, 46
- Schrabback, T., Hartlap, J., Joachimi, B., et al. 2010, A&A, 516, A63
- Scolnic, D. M., Jones, D. O., Rest, A., et al. 2018, ApJ, 859, 101
- Sipp, M., Schäfer, B. M., & Reischke, R. 2021, MNRAS, 501, 683
- Smith, R. E., Peacock, J. A., Jenkins, A., et al. 2003, MNRAS, 341, 1311
- Spergel, D., Gehrels, N., Baltay, C., et al. 2015, arXiv e-prints, arXiv:1503.03757
- Spurio Mancini, A., Reischke, R., Pettorino, V., Schäfer, B. M., & Zumalacárregui, M. 2018, MNRAS, 480, 3725
- Stebbins, A. 1996, arXiv/astro-ph, 9609149
- Sun, L., Fan, Z.-H., Tao, C., et al. 2009, ApJ, 699, 958
- Takada, M. & Jain, B. 2009, MNRAS, 395, 2065
- Takahashi, R., Sato, M., Nishimichi, T., Taruya, A., & Oguri, M. 2012, ApJ, 761, 152
- Taylor, A., Joachimi, B., & Kitching, T. 2013, MNRAS, 432, 1928
- Taylor, P. L., Kitching, T. D., & McEwen, J. D. 2018a, Phys. Rev. D, 98, 043532
- Taylor, P. L., Kitching, T. D., McEwen, J. D., & Tram, T. 2018b, Phys. Rev. D, 98, 023522
- Tessore, N., Loureiro, A., Joachimi, B., von Wietersheim-Kramsta, M., & Jeffrey, N. 2023, The Open Journal of Astrophysics, 6, 11
- Troxel, M. A. & Ishak, M. 2015, Phys. Rep., 558, 1
- Tutusaus, I., Martinelli, M., Cardone, V. F., et al. 2020, A&A, 643, A70
- Upham, R. E., Brown, M. L., & Whittaker, L. 2021, MNRAS, 503, 1999
- Verde, L., Heavens, A. F., Percival, W. J., et al. 2002, MNRAS, 335, 432
- Virtanen, P., Gommers, R., Oliphant, T. E., et al. 2020, Nature Methods, 17, 261
- Xavier, H. S., Abdalla, F. B., & Joachimi, B. 2016, MNRAS, 459, 3693
- Zuntz, J., Lanusse, F., Malz, A. I., et al. 2021, The Open Journal of Astrophysics, 4, 13
- Zuntz, J., Paterno, M., Jennings, E., et al. 2015, Astronomy and Computing, 12, 45
- <sup>1</sup> Jodrell Bank Centre for Astrophysics, Department of Physics and Astronomy, University of Manchester, Oxford Road, Manchester M13 9PL, UK
- <sup>2</sup> School of Mathematics and Physics, University of Surrey, Guildford, Surrey, GU2 7XH, UK
- <sup>3</sup> INAF-Osservatorio Astronomico di Brera, Via Brera 28, 20122 Milano, Italy
- <sup>4</sup> IFPU, Institute for Fundamental Physics of the Universe, via Beirut 2, 34151 Trieste, Italy
- <sup>5</sup> INAF-Osservatorio Astronomico di Trieste, Via G. B. Tiepolo 11, 34143 Trieste, Italy
- <sup>6</sup> INFN, Sezione di Trieste, Via Valerio 2, 34127 Trieste TS, Italy
- <sup>7</sup> SISSA, International School for Advanced Studies, Via Bonomea 265, 34136 Trieste TS, Italy
- <sup>8</sup> Dipartimento di Fisica e Astronomia, Università di Bologna, Via Gobetti 93/2, 40129 Bologna, Italy
- <sup>9</sup> INAF-Osservatorio di Astrofisica e Scienza dello Spazio di Bologna, Via Piero Gobetti 93/3, 40129 Bologna, Italy
- <sup>10</sup> INFN-Sezione di Bologna, Viale Berti Pichat 6/2, 40127 Bologna, Italy
- <sup>11</sup> INAF-Osservatorio Astrofisico di Torino, Via Osservatorio 20, 10025 Pino Torinese (TO), Italy
- <sup>12</sup> Dipartimento di Fisica, Università di Genova, Via Dodecaneso 33, 16146, Genova, Italy
- <sup>13</sup> INFN-Sezione di Genova, Via Dodecaneso 33, 16146, Genova, Italy
- <sup>14</sup> Department of Physics "E. Pancini", University Federico II, Via Cinthia 6, 80126, Napoli, Italy
- <sup>15</sup> INAF-Osservatorio Astronomico di Capodimonte, Via Moirariello 16, 80131 Napoli, Italy
- <sup>16</sup> INFN section of Naples, Via Cinthia 6, 80126, Napoli, Italy
- <sup>17</sup> Instituto de Astrofísica e Ciências do Espaço, Universidade do Porto, CAUP, Rua das Estrelas, PT4150-762 Porto, Portugal
- <sup>18</sup> Faculdade de Ciências da Universidade do Porto, Rua do Campo de Alegre, 4150-007 Porto, Portugal
- <sup>19</sup> Aix-Marseille Université, CNRS, CNES, LAM, Marseille, France
- <sup>20</sup> Dipartimento di Fisica, Università degli Studi di Torino, Via P. Giuria 1, 10125 Torino, Italy
- <sup>21</sup> INFN-Sezione di Torino, Via P. Giuria 1, 10125 Torino, Italy
- <sup>22</sup> INAF-IASF Milano, Via Alfonso Corti 12, 20133 Milano, Italy
- <sup>23</sup> Centro de Investigaciones Energéticas, Medioambientales y Tecnológicas (CIEMAT), Avenida Complutense 40, 28040 Madrid, Spain
- <sup>24</sup> Port d'Informació Científica, Campus UAB, C. Albareda s/n, 08193 Bellaterra (Barcelona), Spain
- <sup>25</sup> Institute for Theoretical Particle Physics and Cosmology (TTK), RWTH Aachen University, 52056 Aachen, Germany
- <sup>26</sup> Institute of Cosmology and Gravitation, University of Portsmouth, Portsmouth PO1 3FX, UK
- <sup>27</sup> INAF-Osservatorio Astronomico di Roma, Via Frascati 33, 00078 Monteporzio Catone, Italy
- <sup>28</sup> Dipartimento di Fisica e Astronomia "Augusto Righi" - Alma Mater Studiorum Università di Bologna, Viale Berti Pichat 6/2, 40127 Bologna, Italy
- <sup>29</sup> Instituto de Astrofísica de Canarias, Calle Vía Láctea s/n, 38204, San Cristóbal de La Laguna, Tenerife, Spain
- <sup>30</sup> Institute for Astronomy, University of Edinburgh, Royal Observatory, Blackford Hill, Edinburgh EH9 3HJ, UK
- <sup>31</sup> European Space Agency/ESRIN, Largo Galileo Galilei 1, 00044 Frascati, Roma, Italy
- <sup>32</sup> ESAC/ESA, Camino Bajo del Castillo, s/n., Urb. Villafraña del Castillo, 28692 Villanueva de la Cañada, Madrid, Spain
- <sup>33</sup> Université Claude Bernard Lyon 1, CNRS/IN2P3, IP2I Lyon, UMR 5822, Villeurbanne, F-69100, France
- <sup>34</sup> Institut de Ciències del Cosmos (ICCUB), Universitat de Barcelona (IEEC-UB), Martí i Franquès 1, 08028 Barcelona, Spain
- <sup>35</sup> Institució Catalana de Recerca i Estudis Avançats (ICREA), Passeig de Lluís Companys 23, 08010 Barcelona, Spain
- <sup>36</sup> UCB Lyon 1, CNRS/IN2P3, IUF, IP2I Lyon, 4 rue Enrico Fermi, 69622 Villeurbanne, France

- <sup>37</sup> Departamento de Física, Faculdade de Ciências, Universidade de Lisboa, Edifício C8, Campo Grande, PT1749-016 Lisboa, Portugal
- <sup>38</sup> Instituto de Astrofísica e Ciências do Espaço, Faculdade de Ciências, Universidade de Lisboa, Campo Grande, 1749-016 Lisboa, Portugal
- <sup>39</sup> Department of Astronomy, University of Geneva, ch. d'Ecogia 16, 1290 Versoix, Switzerland
- <sup>40</sup> INAF-Istituto di Astrofisica e Planetologia Spaziali, via del Fosso del Cavaliere, 100, 00100 Roma, Italy
- <sup>41</sup> INFN-Padova, Via Marzolo 8, 35131 Padova, Italy
- <sup>42</sup> Université Paris-Saclay, Université Paris Cité, CEA, CNRS, AIM, 91191, Gif-sur-Yvette, France
- <sup>43</sup> Space Science Data Center, Italian Space Agency, via del Politecnico snc, 00133 Roma, Italy
- <sup>44</sup> Universitäts-Sternwarte München, Fakultät für Physik, Ludwig-Maximilians-Universität München, Scheinerstrasse 1, 81679 München, Germany
- <sup>45</sup> Aix-Marseille Université, CNRS/IN2P3, CPPM, Marseille, France
- <sup>46</sup> INAF-Osservatorio Astronomico di Padova, Via dell'Osservatorio 5, 35122 Padova, Italy
- <sup>47</sup> Max Planck Institute for Extraterrestrial Physics, Giessenbachstr. 1, 85748 Garching, Germany
- <sup>48</sup> Dipartimento di Fisica "Aldo Pontremoli", Università degli Studi di Milano, Via Celoria 16, 20133 Milano, Italy
- <sup>49</sup> Institute of Theoretical Astrophysics, University of Oslo, P.O. Box 1029 Blindern, 0315 Oslo, Norway
- <sup>50</sup> Jet Propulsion Laboratory, California Institute of Technology, 4800 Oak Grove Drive, Pasadena, CA, 91109, USA
- <sup>51</sup> Department of Physics, Lancaster University, Lancaster, LA1 4YB, UK
- <sup>52</sup> Felix Hormuth Engineering, Goethestr. 17, 69181 Leimen, Germany
- <sup>53</sup> Technical University of Denmark, Elektrovej 327, 2800 Kgs. Lyngby, Denmark
- <sup>54</sup> Cosmic Dawn Center (DAWN), Denmark
- <sup>55</sup> Université Paris-Saclay, CNRS/IN2P3, IJCLab, 91405 Orsay, France
- <sup>56</sup> Institut de Recherche en Astrophysique et Planétologie (IRAP), Université de Toulouse, CNRS, UPS, CNES, 14 Av. Edouard Belin, 31400 Toulouse, France
- <sup>57</sup> Max-Planck-Institut für Astronomie, Königstuhl 17, 69117 Heidelberg, Germany
- <sup>58</sup> NASA Goddard Space Flight Center, Greenbelt, MD 20771, USA
- <sup>59</sup> Department of Physics and Helsinki Institute of Physics, Gustaf Hällströmin katu 2, 00014 University of Helsinki, Finland
- <sup>60</sup> Université de Genève, Département de Physique Théorique and Centre for Astroparticle Physics, 24 quai Ernest-Ansermet, CH-1211 Genève 4, Switzerland
- <sup>61</sup> Department of Physics, P.O. Box 64, 00014 University of Helsinki, Finland
- <sup>62</sup> Helsinki Institute of Physics, Gustaf Hällströmin katu 2, University of Helsinki, Helsinki, Finland
- <sup>63</sup> NOVA optical infrared instrumentation group at ASTRON, Oude Hoogeveensedijk 4, 7991PD, Dwingeloo, The Netherlands
- <sup>64</sup> Centre de Calcul de l'IN2P3/CNRS, 21 avenue Pierre de Coubertin 69627 Villeurbanne Cedex, France
- <sup>65</sup> Universität Bonn, Argelander-Institut für Astronomie, Auf dem Hügel 71, 53121 Bonn, Germany
- <sup>66</sup> INFN-Sezione di Roma, Piazzale Aldo Moro, 2 - c/o Dipartimento di Fisica, Edificio G. Marconi, 00185 Roma, Italy
- <sup>67</sup> Dipartimento di Fisica e Astronomia "Augusto Righi" - Alma Mater Studiorum Università di Bologna, via Piero Gobetti 93/2, 40129 Bologna, Italy
- <sup>68</sup> Department of Physics, Institute for Computational Cosmology, Durham University, South Road, Durham, DH1 3LE, UK
- <sup>69</sup> Université Paris Cité, CNRS, Astroparticule et Cosmologie, 75013 Paris, France
- <sup>70</sup> University of Applied Sciences and Arts of Northwestern Switzerland, School of Engineering, 5210 Windisch, Switzerland
- <sup>71</sup> Institut d'Astrophysique de Paris, 98bis Boulevard Arago, 75014, Paris, France
- <sup>72</sup> Institut d'Astrophysique de Paris, UMR 7095, CNRS, and Sorbonne Université, 98 bis boulevard Arago, 75014 Paris, France
- <sup>73</sup> Institute of Physics, Laboratory of Astrophysics, Ecole Polytechnique Fédérale de Lausanne (EPFL), Observatoire de Sauverny, 1290 Versoix, Switzerland
- <sup>74</sup> Institut de Física d'Altes Energies (IFAE), The Barcelona Institute of Science and Technology, Campus UAB, 08193 Bellaterra (Barcelona), Spain
- <sup>75</sup> European Space Agency/ESTEC, Keplerlaan 1, 2201 AZ Noordwijk, The Netherlands
- <sup>76</sup> DARK, Niels Bohr Institute, University of Copenhagen, Jagtvej 155, 2200 Copenhagen, Denmark
- <sup>77</sup> Centre National d'Etudes Spatiales – Centre spatial de Toulouse, 18 avenue Edouard Belin, 31401 Toulouse Cedex 9, France
- <sup>78</sup> Institute of Space Science, Str. Atomistilor, nr. 409 Măgurele, Ilfov, 077125, Romania
- <sup>79</sup> Dipartimento di Fisica e Astronomia "G. Galilei", Università di Padova, Via Marzolo 8, 35131 Padova, Italy
- <sup>80</sup> Institut für Theoretische Physik, University of Heidelberg, Philosophenweg 16, 69120 Heidelberg, Germany
- <sup>81</sup> Université St Joseph; Faculty of Sciences, Beirut, Lebanon
- <sup>82</sup> Departamento de Física, FCFM, Universidad de Chile, Blanco Encalada 2008, Santiago, Chile
- <sup>83</sup> Universität Innsbruck, Institut für Astro- und Teilchenphysik, Technikerstr. 25/8, 6020 Innsbruck, Austria
- <sup>84</sup> Institut d'Estudis Espacials de Catalunya (IEEC), Edifici RDIT, Campus UPC, 08860 Castelldefels, Barcelona, Spain
- <sup>85</sup> Satlantis, University Science Park, Sede Bld 48940, Leioa-Bilbao, Spain
- <sup>86</sup> Institute of Space Sciences (ICE, CSIC), Campus UAB, Carrer de Can Magrans, s/n, 08193 Barcelona, Spain
- <sup>87</sup> Instituto de Astrofísica e Ciências do Espaço, Faculdade de Ciências, Universidade de Lisboa, Tapada da Ajuda, 1349-018 Lisboa, Portugal
- <sup>88</sup> Universidad Politécnica de Cartagena, Departamento de Electrónica y Tecnología de Computadoras, Plaza del Hospital 1, 30202 Cartagena, Spain
- <sup>89</sup> INFN-Bologna, Via Irnerio 46, 40126 Bologna, Italy
- <sup>90</sup> Kapteyn Astronomical Institute, University of Groningen, PO Box 800, 9700 AV Groningen, The Netherlands
- <sup>91</sup> Dipartimento di Fisica, Università degli studi di Genova, and INFN-Sezione di Genova, via Dodecaneso 33, 16146, Genova, Italy
- <sup>92</sup> Infrared Processing and Analysis Center, California Institute of Technology, Pasadena, CA 91125, USA
- <sup>93</sup> INAF, Istituto di Radioastronomia, Via Piero Gobetti 101, 40129 Bologna, Italy
- <sup>94</sup> Astronomical Observatory of the Autonomous Region of the Aosta Valley (OAVdA), Loc. Lignan 39, I-11020, Nus (Aosta Valley), Italy
- <sup>95</sup> ICL, Junia, Université Catholique de Lille, LITL, 59000 Lille, France
- <sup>96</sup> Department of Physics, Royal Holloway, University of London, TW20 0EX, UK
- <sup>97</sup> ICSC - Centro Nazionale di Ricerca in High Performance Computing, Big Data e Quantum Computing, Via Magnanelli 2, Bologna, Italy

## Appendix A: Results and validation

In this section we present the validation framework with which we investigate the accuracy of our simulation method to reproduce a target tomographic 3×2pt signal for both a no-noise and noisy setup. We examine the 3×2pt Pseudo- $C_\ell$  power spectra measured over 400 realisations of our mock catalogues, and demonstrate that the sample generated by our pipeline can self-consistently reproduce the underlying power spectra predicted by the input cosmology to an encouraging accuracy. For our validation framework, we adopt the simulation setup parameters that are defined at the start of Sect. 6, and measure the Pseudo- $C_\ell$  power spectra using 10 log-spaced bandpowers in the range  $100 \leq \ell \leq 1500$ .

### Appendix A.1: No-noise simulation

For our first-order validation demonstration, we present results for a ‘no-noise’ simulation which includes no systematic contribution from redshift uncertainty or shape noise. In Fig. A.1 we present the binned  $n(z)$  for this validation tomography and the corresponding measurements of the Pseudo- $C_\ell$  bandpowers of the data for each of the 3×2pt components. Alongside, we plot the theoretical prediction, constructed using Eqs. (33–37), and the normalised (fractional) residuals for each spectrum, which we denote as  $\Delta_f$ . We calculate the errorbars using the standard deviation of the data points measured from the 400 realisations.

In general, we find that for the ‘no-noise’ setup, the 3×2pt measurements from our catalogues show very good agreement with the fiducial model. Collectively, the residuals of the 3×2pt data vector demonstrate that our method can accurately reconstruct the underlying 3×2pt signal to sub-percent accuracy, which we highlight as a very encouraging performance of our simulation approach.

Comparatively, the galaxy clustering power spectra show that the measured signal in the auto-correlation bins shows a minimal ( $\sim 0.5\%$ ) under-recovery with respect to the theoretical prediction. This behaviour is not present in the shear or galaxy-galaxy lensing power spectrum, which both show a more random scatter about the model. Additionally, we note that for a no-noise simulation, in which source galaxy redshifts are estimated with complete precision, there is no overlap between the redshift distributions of different tomographic bins. Hence, the cross-correlation power spectra of the galaxy clustering signal, and the galaxy-galaxy lensing cross spectra, in which a foreground (low redshift) shear field is correlated with a background clustering field, each have extremely low signal. The corresponding normalised residuals are therefore extremely large due to the small number statistics associated with the very small quantities.

### Appendix A.2: Realistic, ‘noisy’ realisations with shape noise and photo- $z$ uncertainty

In this section we present results of the 3×2pt Pseudo- $C_\ell$  power spectra measured from our simulated mock catalogues that now include contributions from shape noise and photometric redshift estimation uncertainty. We model the uncertainties arising from each of these sources using Gaussian-distributed errors, taking  $\sigma(\epsilon^{\text{int}}) = 0.3$  and  $\sigma_z^{\text{phot}} = 0.05$  as defined in Sect. 6.

In Fig. A.2 we present the bandpowers of the 3×2pt Pseudo- $C_\ell$  power spectra measured over 400 simulations using the same validation framework of three bins equipopulated with galaxies as considered in the no-noise case in Appendix A.1. We show

the normalised residuals under each power spectrum component in Fig. A.2, and present the binned  $n(z)$  in the upper left corner.

We find that the 3×2pt power spectra measured from the simulated noisy catalogues are in good general agreement with the theoretical prediction. In the presence of Gaussian shape noise and photo- $z$  errors, the shear and galaxy-galaxy lensing signals both show a similar level of recovery of the fiducial model, at the  $\sim 1\%$  level. This is consistent with that seen in the noise-free 3×2pt simulations. However, for the galaxy clustering, the measured auto-correlation power spectra are consistently  $\sim 2\%$  lower than the prediction from the theoretical model. This is significantly larger than the  $\sim 0.5\%$  deficit found in the corresponding no-noise simulations. Furthermore, the cross-correlation power spectra between bins are in more considerable disagreement, with the recovered power spectra being 5–6% in excess of the theoretical prediction. While the absolute values of these cross spectra are over a magnitude smaller than the auto-correlation signals, this 5–6% level discrepancy in the cross-correlation clustering power spectra represents the limiting precision of our simulation approach.

We attribute the above discrepancies to a small (but non-negligible) fundamental inconsistency between our simulation process and our model predictions. The former is an attempt to simulate the full 3D distribution and evolution of matter in the Universe, approximating it as a stack of 2D fields on the sky that have been evaluated using a tomographic projection over finely-binned, discretised points in redshift. The resulting catalogues are then binned into much broader redshift bins for the cosmological power spectrum analysis. In contrast, the theoretical model directly predicts the signal in these much broader redshift bins, again using a tomographic projection but now performing the Limber integration over a much broader redshift kernel (see Eqs. 1–6). Consequently, our simulation and modelling approaches contain different levels of approximation. This is the fundamental reason for the small discrepancies described above. Furthermore, one expects that the disagreement would be exacerbated in the presence of photometric redshift errors, which is what we have found.

## Appendix B: Correction factors and robustness validation of the numerical covariance matrix

For our Gaussian likelihood analysis to derive 3×2pt constraints on  $(w_0, w_a)$  we use a numerical covariance matrix where we retain only the diagonals of each block (see Sect. 5). The numerical covariance matrix directly quantifies the errors associated with our simulation method, but it will also contain excess random noise associated with the finite number of simulations used (see e.g. Dodelson & Schneider 2013, Taylor et al. 2013 for further discussion). In the limit of an infinite number of realisations available, this noise will average to zero and leave only the ‘true’ information in the covariance matrix.

Since we can only work with a finite number of realisations, we investigate the impact that the excess noise has on the  $(w_0, w_a)$  contours derived from our measurements. Firstly, we demonstrate that the random noise suppresses the true signal most damagingly in the off-diagonal elements of each block, which motivates us to filter out these components and use a ‘block-diagonal’ covariance matrix to derive the cosmological constraints in our analysis. Secondly, we derive ‘correction factors’ that quantify the degree to which the signal in the retained block-diagonal elements is suppressed with respect to a covariance matrix derived from a much higher number of simulations, where we interpret the latter as the shot noise-free covariance.

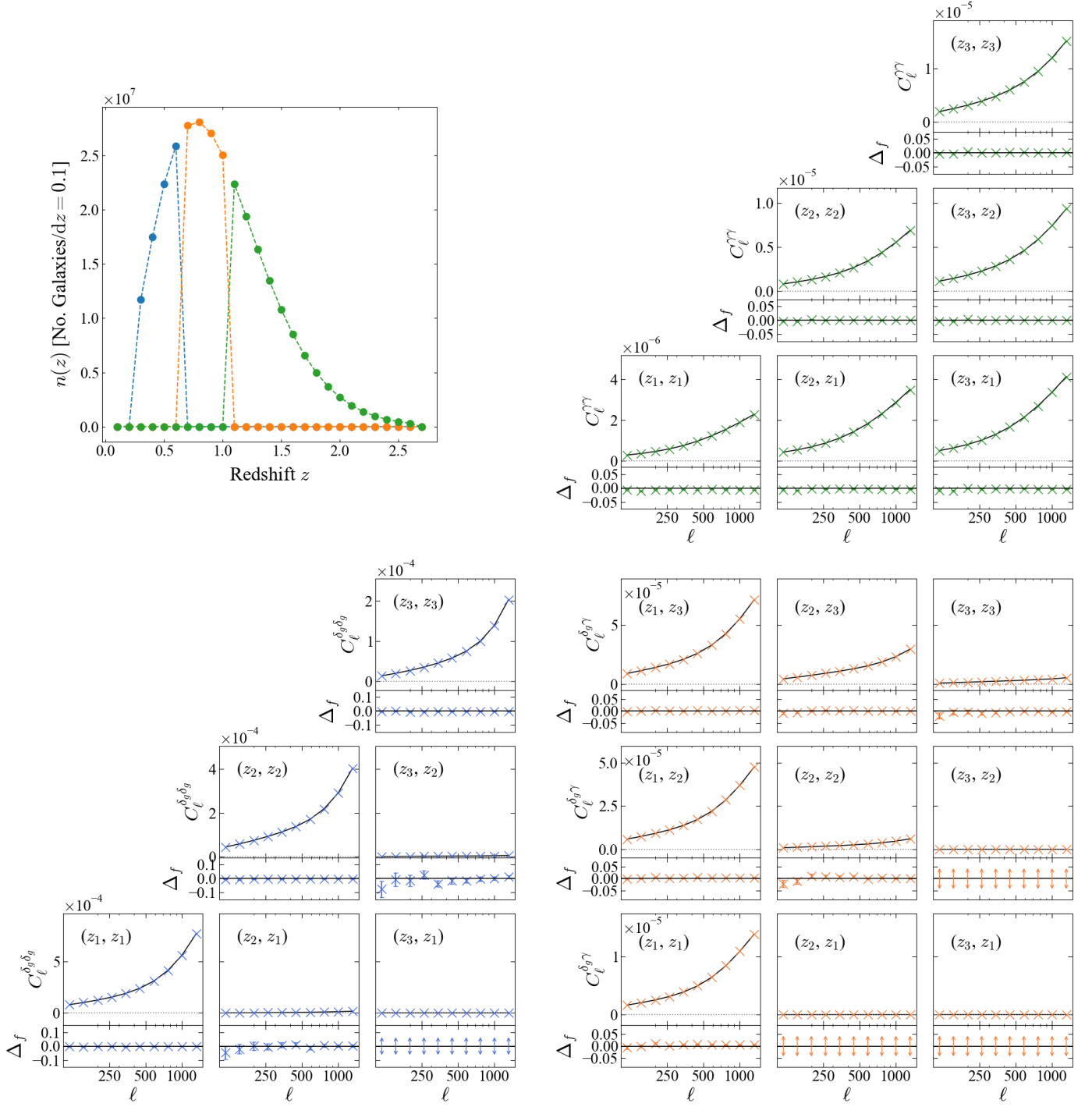


**Fig. A.1.** **Top Left:** The binned  $n(z)$  for a tomographic  $3\times 2$ pt analysis of our mock catalogues using 3 equipopulated bins, with no contribution from shape noise or photo- $z$  uncertainty in the simulation. **Top Right, Bottom Left, Bottom Right:** The measured  $3\times 2$ pt Pseudo- $C_\ell$  power spectra (cosmic shear, angular clustering, galaxy-galaxy lensing, respectively) measured over 400 realisations for this chosen tomography, shown in crosses. We bin the power spectra into 10 log-spaced bandpowers and measure the signal in the range  $100 < \ell < 1500$ . The solid black lines show the input model power spectra. Beneath each individual power spectrum we plot the normalised residuals of the data, defined as the fractional quantity  $(C_\ell^{\text{Measured}}/C_\ell^{\text{Theory}}) - 1$ , which we denote as  $\Delta_f$  on the y-axis label. The vertical double-headed arrows in the off-diagonal subplots indicate that the fractional residuals, and their errors, for these spectra are extremely large due to the division by an extremely small signal.

In order to quantify these points, we modify our simulation and analysis approach into the following steps.

- Generate correlated  $3\times 2$ pt fields on the sky for a pre-determined target tomographic binning configuration.
- Generate per-bin realisations of the realistic noise components – Poisson noise in the angular clustering and shape noise in the cosmic shear – and inject into the  $3\times 2$ pt fields.
- Measure the  $3\times 2$ pt power spectra from the combined signal + noise maps using the same Pseudo- $C_\ell$  approach as Sect. 3.2, and propagate into the Gaussian likelihood analy-



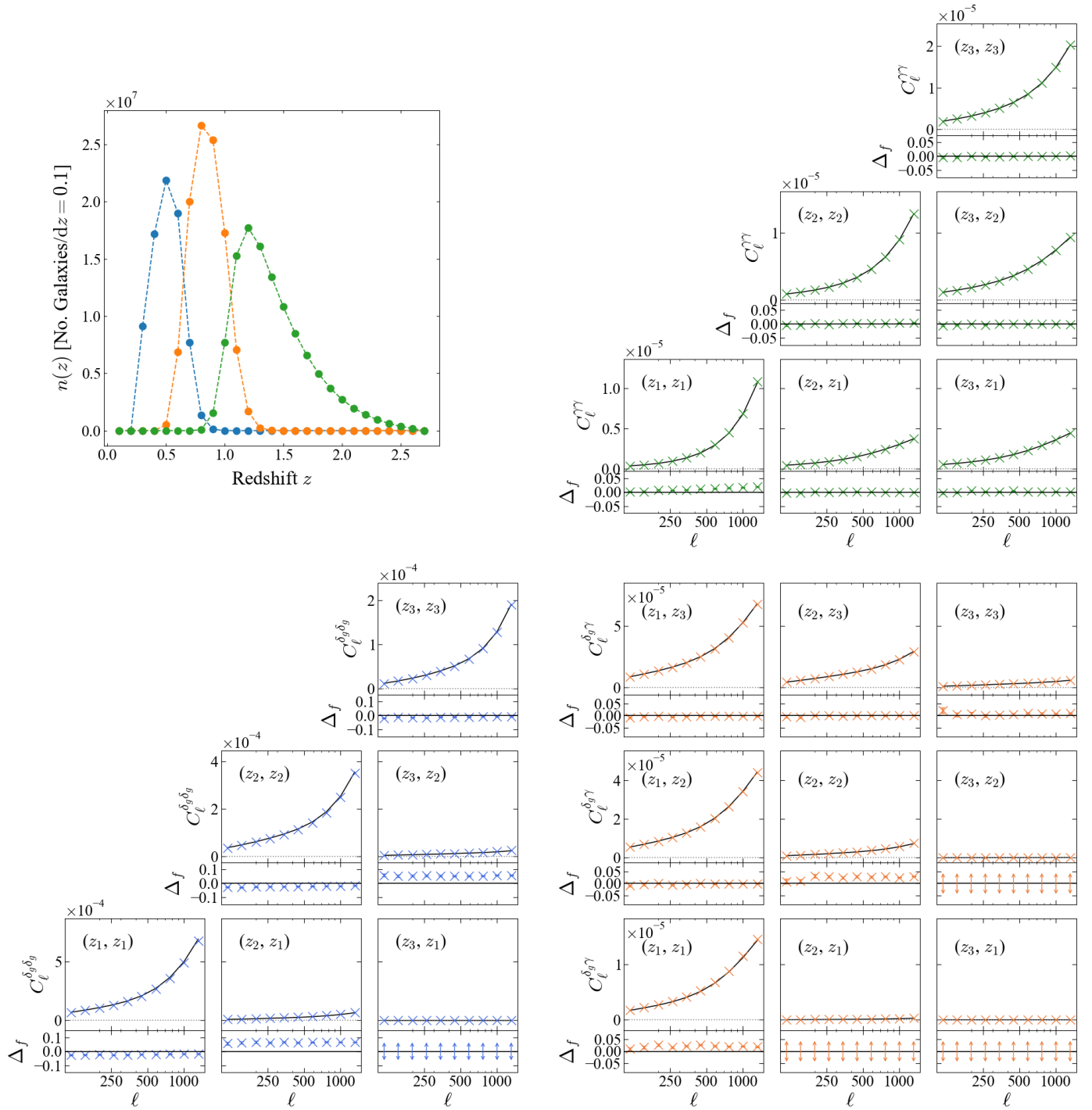


**Fig. A.2.** **Top Left:** The binned  $n(z)$  for a 3 equipopulated bin tomographic setup, measured from our mock catalogues that include realistic Gaussian shape noise and photo- $z$  uncertainties in the simulation. **Top Right, Bottom Left, Bottom Right:** The cosmic shear, angular clustering and galaxy-galaxy lensing components (respectively) of the 3×2pt data vector. We show in crosses the Pseudo- $C_\ell$  power spectra measured over 400 realisations of our simulation for this chosen tomography. We bin the multipoles into 10 log-spaced bandpowers and measure the signal in the range  $100 < \ell < 1500$ . We plot the theoretical prediction in black alongside the measured data, and underneath each individual power spectrum we plot the normalised residuals, which we define as the fractional quantity  $(C_\ell^{\text{Measured}}/C_\ell^{\text{Theoretical}}) - 1$ , denoted as  $\Delta_f$  on the y-axis label.

sis of Sect. 5 to determine the constraints on the dark energy  $(w_0, w_a)$  parameters.

This is a simplified reconstruction of what is executed in our full simulation pipeline but we benefit greatly from a significantly reduced computational cost. We use this modified analysis pipeline for a sample of the tomographic binning configurations explored

in our main study. For these cases, we measure the  $(w_0, w_a)$  contour areas derived as a function of the realisations included in the simulation, evaluated for both the full covariance matrix and for the filtered block-diagonal covariance matrix.

We present these results for analyses using a single redshift bin, 5 equipopulated bins, and 10 equipopulated bins, in Fig. B.1. We show in blue and orange the  $(w_0, w_a)$  areas for the 1 and 2  $\sigma$

contours respectively, and in solid and dashed lines the measurements from the full covariance matrix and the block-diagonal covariance matrix respectively.

We find that for a single tomographic bin, the  $(w_0, w_a)$  contours determined from the full covariance matrix converge to a consistent value by  $\sim 500$  realisations, while measurements from the block-diagonal covariance converge much more quickly, at  $\sim 200$  realisations. Comparatively, by 2000 realisations, the block-diagonal recovers  $\sim 90\%$  of the information contained in the full numerical covariance matrix, which would indicate that our measurements on  $(w_0, w_a)$  for the single tomographic redshift bin underestimate the true errors by  $\sim 10\%$ .

In contrast, for the analysis using 5 equipopulated bins we see that even by 2000 realisations the area enclosed in  $(w_0, w_a)$  by the full covariance matrix has not converged, but for the block-diagonal case the convergence is achieved by  $\sim 1000$  realisations. Importantly, this result suggests that we cannot rely on using the full covariance matrix, since it is likely we would need  $\mathcal{O}(10\,000)$  realisations to achieve stable behaviour in the  $(w_0, w_a)$  contours. This is impractical to achieve in our full catalogue simulation which is more computationally demanding than this simplified investigation, and would motivate an attempt to filter out the noise that is limiting the convergence to stable behaviour. Additionally, the contour areas derived from the block-diagonal covariance matrix converge relatively quickly in comparison, which indicates that this is a good filtering choice to make. Moreover, we can calculate the ratio of the area of the  $(w_0, w_a)$  contours derived from the block-diagonal covariance matrix at 2000 realisations compared to the area at 400 realisations to estimate the underprediction in the errors that we might be making in our main analysis.

These conclusions are further consolidated in the 10 bin analysis, where we find that the full covariance matrix even at 2000 realisations is too noisy to invert and derive stable  $(w_0, w_a)$  constraints. Comparatively, measurements of the  $(w_0, w_a)$  areas using the block-diagonal covariance matrix perform more reasonably and start to converge at  $\geq 2000$  realisations. However, we note that this is still an excessively large number of realisations to manipulate for our main analysis, which motivates using a smaller number of realisations with the block-diagonal covariance, and then correcting for any noise still present in the filtered matrix by taking the ratio of the  $(w_0, w_a)$  area at 2000 realisations to the area at 400 realisations in Fig. B.1.

We define this ratio as the ‘correction factor’ and plot in the bottom panel of Fig. B.2 these factors measured for the 1 and  $2\sigma$   $(w_0, w_a)$  areas as a function of the number of tomographic bins used for a  $3\times 2$ pt analysis, for each of the three different binning choices considered in this work.

We find that the correction factors increase as the number of redshift bins increases, which is an expected result since the  $3\times 2$ pt data vector thus becomes longer and more prone to noise. Additionally, the correction factors are largest for the equipopulated binning, followed by the equal redshift width and equal comoving distance choices, which represents the order of significance of the random noise level that is still present in the block-diagonal covariance matrix at 400 realisations, across the three binning choices. Nonetheless, we emphasise that the difference in the correction factors between the binning choices for a given number of redshift bins is only a few percent, which indicates that the dependence of the correction factor on the binning choice is relatively weak.

In order to correct the measurements of  $(w_0, w_a)$  presented in our main analysis, for every given tomographic setup, we multiply the measured posterior contour areas by the correction factor

read off in Fig. B.2 for the same tomographic binning choice and number of redshift bins considered.

In addition to the full  $3\times 2$ pt data vector, we repeat the analysis of the realisation-dependent behaviour of the numerical covariance matrix for both of the noisy cosmic shear and angular clustering signals and plot the correction factors that we apply for each of these signals in the top and middle panels of Fig. B.2. For each of the  $3\times 2$ pt components we then choose to use the same noise-like correction factors for the no-noise measurements, for the ease of computational cost. The effect of including the Gaussian shape noise and photo- $z$  uncertainty is to increase the random noise present in the numerical covariance matrix, hence the correction factors for the noisy case would be greater in magnitude than for the no-noise case. Consequently, applying the noise-like correction factors to the no-noise analysis represents a conservative approach to examine the efficacy of our method. We find that this results in no change to the final conclusions on the no-noise measurements in the main study, which indicates that they are robust regardless of the inclusion of any correction factor.

Furthermore, we note that due to the practical computational limitations we do not evaluate the correction factors for every single tomographic setup explored in this work, but rather focus on measuring a sample of correction factors per binning choice and interpolate between these measurements to find the intermediate values.

Explicitly, since the correction factors increase with the number of tomographic redshift bins used, the main effect that they introduce to the measurements is a slight change in the shape of the curves showing the  $(w_0, w_a)$  contour areas as a function of the number of redshift bins (Figs. 3, 4, 5, 7, 9, 11, in which these correction factors have been applied). On inclusion of the correction factors, the curves exhibit a slightly clearer flattening whereby the  $(w_0, w_a)$  areas start to converge to a consistent value at  $\sim 6$ – $8$  redshift bins, indicating that this may be the point at which information gain starts to saturate when increasing the number of redshift bins used for the tomographic analysis.

However, we emphasise that the correction factors do not change the order of preference of the binning choices (e.g. as summarised in Table 1) for any  $3\times 2$ pt component both with and without noise included. Consequently, these results indicate that our conclusions on the optimum binning choice for each observable and noise scenario are robust.

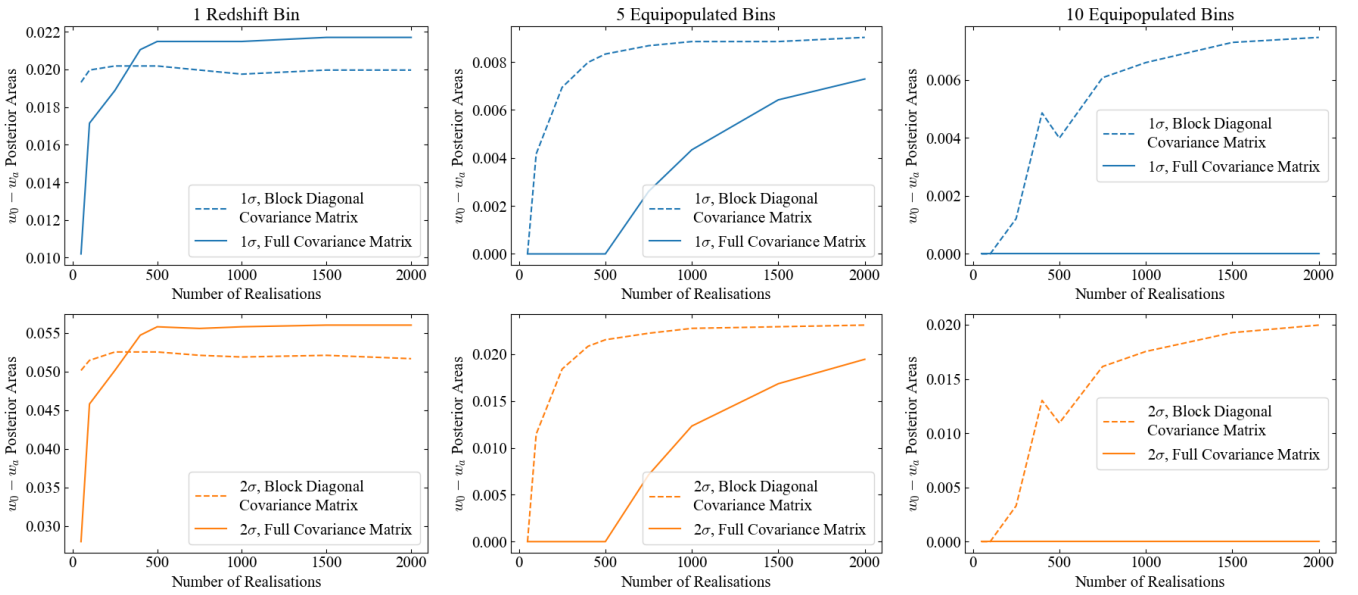


**Fig. B.1.** The areas of the 1 and 2  $\sigma$  constraints on  $(w_0, w_a)$  for a full 3×2pt analysis adopting the simplified simulation method discussed in Appendix B, which we use to investigate the robustness of the covariance matrix used in the main study. We show the contour areas measured as a function of the number of realisations included while using: **Solid Line**) the full numerical covariance, and **Dashed Line**) only the ‘block-diagonal’ elements of the numerical covariance matrix in the inference routine. From left to right we present these measurements for tomographic measurements using a single redshift bin, 5 equipopulated bins, and 10 equipopulated bins.

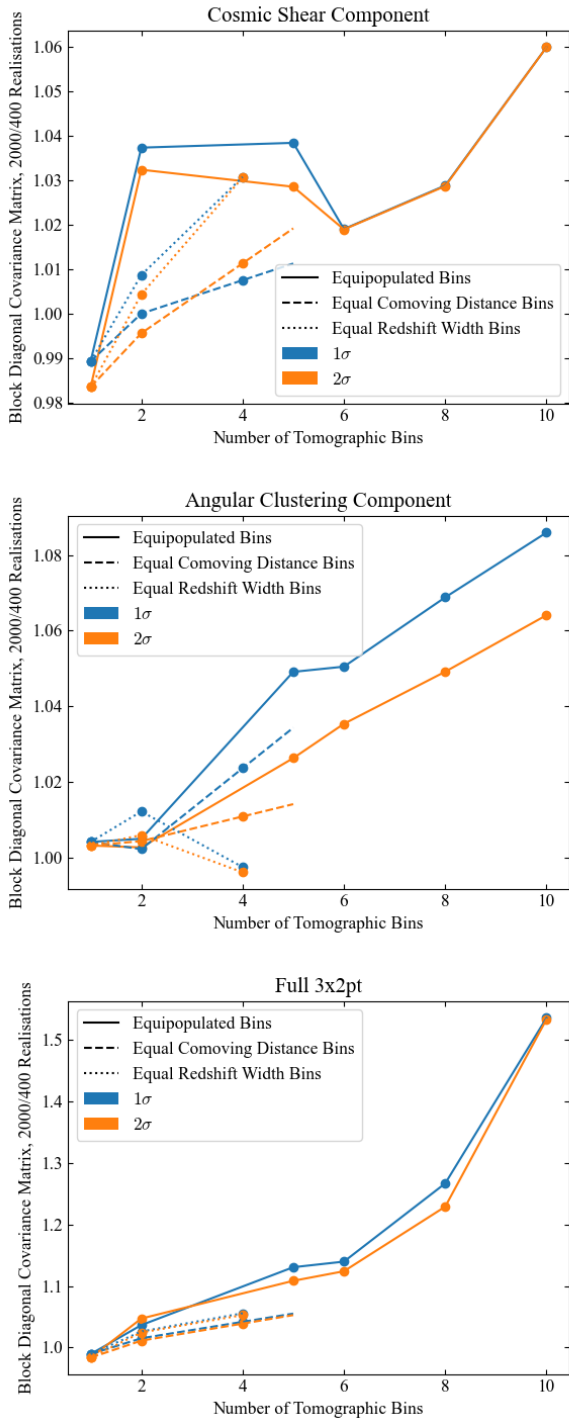


**Fig. B.2.** The ratio of the 1 and 2  $\sigma$  ( $w_0, w_a$ ) contour areas derived from using the block-diagonal covariance matrix, for 2000 realisations compared to 400 realisations in our simplified simulation. These ratios represent the ‘correction factors’ that describe the excess level of random noise in the covariance matrix that results from using 400 realisations in the main study, which leads to overly optimistic constraints on ( $w_0, w_a$ ). We show the correction factors for the three different tomographic binning choices considered throughout the work, for several different numbers of redshift bins in the range 1–10, which we interpolate between to derive intermediate values. From top to bottom, we plot the correction factors derived for the cosmic shear signal, the angular clustering component, and the full 3 $\times$ 2pt signal for a noisy simulation. Consequently, we apply the relevant correction factors to measurements of the ( $w_0, w_a$ ) contours in the main study but find that they do not influence any overall conclusions.